Modeling and Simulation of Third Party Risk of an Unmanned Aircraft Systems-based Surveillance Operation in the Port of Rotterdam

J.E. Vettorato

Delft University of Technology

Port of Rotterdam

TU Delft

Modeling and Simulation of Third Party Risk of an Unmanned Aircraft Systems-based Surveillance Operation in the Port of Rotterdam

by

J.E. Vettorato

Final thesis

Faculty of Aerospace Engineering, Department of Control & Operations,

Profile of Air Transport & Operations.

Student number:	4099060	
Project duration:	October 1, 2019 – March 11, 2021	
Supervisors:	Prof. dr. ir. H.A.P. Blom	Delft University of Technology
	MSc I.I.E.M. Römers	Port of Rotterdam Authority
Additional committee:	Dr. G.C.H.E. de Croon (Chair)	Delft University of Technology
	Dr. O.A. Sharpanskykh	Delft University of Technology

An electronic version of this thesis is available at `http://repository.tudelft.nl/`.

TU Delft

Abstract

Operations by unmanned aircraft systems (UAS) or 'drones' pose third party risks to persons on the ground. The key question is: are these third party risks acceptably low? This thesis evaluates the level of risk posed by a concept UAS surveillance-based operation in the port of Rotterdam, by means of modeling and simulation.

In a preceding MSc thesis, a modeling and simulation approach to estimate third party risk posed by a drone-based parcel delivery service is researched. This modeling and simulation approach has been extended in quite a number of directions. Firstly, the details of the intended drone-based surveillance operation have been defined in collaboration with the Port of Rotterdam Authority. Secondly, the dynamic model of a quadcopter has been replaced by a dynamic model of a fixed-wing UAS. Thirdly, the influence of wind turbulence on the stochastic deviations of the drone flight have been modeled. Fourthly, for the seaport area a method has been developed for estimating local population densities, rather than using census-based data. These models have been integrated in a Monte Carlo (MC) simulation of the intended surveillance operation in the port of Rotterdam.

The outcome of the MC simulations shows that the estimated third party risk level posed per drone flight hour to persons on the ground is about a factor 4 higher than a maximal allowable threshold proposed by the Joint Authorities for Rulemaking on Unmanned Systems (JARUS). The simulation results also show that the shallow glide angle of the fixed-wing UAS proposed for the surveillance operation causes a relatively large crash impact area on the ground, which leads to a relatively large expected number of persons to be hit by a ground crash. As expected, the main contributions to third party risk stem from parts of a surveillance flight that are near the city, not from parts towards the sea. Another interesting finding is that the estimated third party risk level remains the same if wind turbulence induced flight deviations are ignored. The modeling and simulation results developed in this thesis provide useful feedback to the further development of drone-based operations in the port of Rotterdam, in terms of UAS characteristics, flight trajectory, and mitigating measures. Follow up research is desired in the fields of failure probability estimation, sheltering probability estimation, and population density estimation.

Preface

With this thesis I conclude my master's degree at the Delft University of Technology. I could not have done this without the support of many persons, to whom I would like to address a few words to express my gratitude.

First of all I would like to thank my TU Delft supervisor, professor Henk Blom, who took me on to graduate under his supervision even after the discontinuation of his chair due to his planned retirement. He allowed me to graduate externally at the wonderful company of the Port of Rotterdam Authority, which has now become my employer. My usual evening emails often received a supportive reply later that same evening.

I would also like to thank my daily supervisor at the Port of Rotterdam Authority, Ingrid Römers, for her guidance, flexibility, and positive mindset, which I could always utilize during challenging times, and I would like to thank the employees of the Port of Rotterdam Authority for allowing me to use their time, and for providing me with company data.

Lastly, a special thanks to all my friends and family for supporting me throughout my studies, and assisting me to keep my thesis up and running during the Covid-19 pandemic.

J.E. Vettorato
Rotterdam, February 2020

Contents

Acronyms

AIS	Abbreviated Injury Scale
ATM	air traffic management
BVLOS	beyond visual line of sight
CBS	Statistics Netherlands
EASA	European Union Aviation Safety Agency
ILT	Human Environment and Transport Inspectorate
JARUS	Joint Authorities for Rulemaking on Unmanned Systems
KNMI	Royal Netherlands Meteorological Institute
MSL	mean sea level
MTOW	maximum take-off weight
TLS	target level of safety
TPR	third party risk
UA	unmanned aircraft
UAS	unmanned aircraft systems
VTOL	vertical take-off and landing

List of Tables

List of Figures

1

Introduction

Before specifying the details of how this research is conducted, this chapter lists general information about recent proceedings and Port of Rotterdam Authority incentives and regulatory needs for added research that led to the initiation of this research.

1.1. Research motivation

On the 8th of July, 2020, the Dutch Ministry of Defense held a trial to perform an unmanned aircraft systems (UAS) night time flight to track down intruders in the Rotterdam seaport terminals. During the flight, the ground pilot lost contact with the aircraft, after which the drone collided with a structure on the terrain of APM Terminal Rotterdam. [Rijnmond, 2020] Although the news article perfectly substantiates the importance of this thesis research, the incident occurred after this thesis was started, and was therefore not a motivation for its initiation. Besides the Delft University of Technology, the other initiator of this thesis assignment is the Port of Rotterdam Authority.

Port of Rotterdam Authority The Port of Rotterdam Authority is a privatized company that manages the commercial position of the Rotterdam harbor by stimulating harbor activities, as well as serving as an authority in the harbor by aiming for a fast, safe, clean and secure way of traffic handling. The company Port of Rotterdam Authority therefore differs from the 'port of Rotterdam' as an area, the term that is used when the area in and around the river is referred to, as well as when the collective of companies residing on the harbor terminals are mentioned. A common misconception should be solved by noting that the Port of Rotterdam Authority itself does not exercise harbor activities such as commercial shipping or cargo handling. All of the Port of Rotterdam Authority commercial activities aim to increase the port area's competitive position, so that a maritime trade businesses might choose the port of Rotterdam as their operating hub. These activities serve commercial incentives, for example, managing and developing the port area, and improving efficiency for maritime businesses. The Port of Rotterdam Authority also performs activities that adhere to their public tasks to supervise, to ensure enforcement of legislation in the harbor area and to handle marine traffic. This

thesis is conducted for the Harbor Master's Division, whose task is to maintain a safe, smooth, sustainable and secure handling of shipping in the port of Rotterdam [Port of Rotterdam, 2019]. One of the Harbor Master's Division's operations to ensure a safe port environment, is supervision. This is performed by multiple Port of Rotterdam Authority patrol vessels that travel the length of the river and river basins to guard safety and compliance of all parties, and to assist in case of emergencies. One of the most valuable contributions of the patrol vessels is to have eyes pointed at different locations throughout the harbor area. The number of ships available at all times ensures coverage of the entire area, making sure every location is visited at a desired frequency.

Using UAS Even more eyes pointed at the river and river basins can be obtained by using UAS, commonly called 'drones', for this purpose. Two aspects that UAS are perfectly suited for, are to reach remote places quickly, and to offer an excellent bird's-eye view. Because of this they are perfect to assist the patrol vessels in their surveillance operation. This is why the Port of Rotterdam Authority has chosen to explore the possibility of assisting the surveillance operation with UAS. Patrol vessels cannot be replaced fully by UAS, however, because sometimes a closer look is needed, as well as physical assistance, such as fire extinguishing, which can only be provided by marine vessels.

Upcoming regulations Another factor that plays a role in the initiation of this research is that new regulations will be introduced as of 2021 by European Union member states, that are based on the proposal of the [European Commission, 2019a]. The year 2021 will mark the start of a transitional period resulting in new opportunities and functionalities in the operation of unmanned aircraft systems (UAS). During this period the goal is to achieve a level of safety that matches manned aviation, as is the target set by [JARUS, 2015], which name represents the 'Joint Authorities for Rulemaking on Unmanned Systems' and whose methods are advised by European Union Aviation Safety Agency (EASA) for competent authorities to use as a guideline to their national UAS regulations [European Commission, 2019b]. Earlier stages of the implementation phase prescribe the conditions that drone operators should meet to receive approval to conduct operations with higher risk, such as automatic flight. Later stages will offer a fully functional set of services called 'U-space', that automates different tactical aspects of a drone operation, such as flight planning and air traffic management [SESAR JU, 2017]. The further we near to the various initiation stages deadlines, the more need there is for these stages to have been assessed for their safety risk.

1.2. Third party risk

The investigation into the added value of UAS to the Port of Rotterdam Authority surveillance operation, an operation that is currently in its concept phase, starts with researching the effect on safety risk. Safety risk can be expressed in multiple ways, and can be considered separately for the involved parties, as explained below.

Safety risk Safety risk is expressed as a product of likelihood of an event, multiplied with the safety effect of the consequence of that event. In safety risk assessment

negative consequences from the conduction of the operation can be considered, such as damaged property and injury. There are also positive safety risks involved when introducing an operation, where beneficial consequences are evaluated such as the substitution of other hazardous transport methods by the new operation. A typical way of risk quantification for the safety of persons in manned aviation is the expression of the expected number of fatalities divided by the total number of flight hours.

First, second and third parties There are different parties involved in aviation, of which there exist two definitions. For commercial aviation, according to [EUROCONTROL, 2015] the first party is the one providing the air transportation service (aviation personnel), the second party is the party for whom the air transportation is provided (passengers), and the third party are the persons outside the aircraft that are not involved in the operation or maintenance of the aircraft. The main focus of aviation risk research has historically been on first and second parties. [Clothier et al., 2018] define the three different parties for UAS in the following way: First parties are people and property directly associated with the operation, second parties are people and property not associated with the operation, but directly derive benefit from the operation, and finally, third parties are people and property not associated with, nor are deriving direct benefit from the operation. Contrarily to the focus of commercial aviation, the main safety concern of UAS operations is third party risk (TPR) risk [Jiang et al., 2020]. Risk calculation models that are focused on third parties are called TPR models. These models are explained further in chapter 3 and chapter 5.

1.3. Research question

This aim of this research is to quantify the third party risk of the unmanned aircraft systems based surveillance operation in the Port of Rotterdam. Several aspects of the operation influence the total risk level. Based on what is still desired to be researched in current literature in this topic, and based on aspects that accompany this specific operation, a custom scope is determined which defines the research question. The research question is stated as follows:

What is the third party risk of an unmanned aircraft systems-based surveillance operation in the port of Rotterdam, assessed by means of modeling and simulation?

1.4. Report outline

As a first step in the assessment of the operation that is the subject of this thesis, the operation is described in chapter 2. Relevant literature on previous research on safety risk assessment is listed in chapter 3. Potential hazards are described, together with the specific scenario that defines the scope of this research and which safety goal is to be met. The goal and scope are stated in chapter 4. A description of the methodology and the model applied for the simulation of the safety level of the operation are given in chapter 5. This methodology is verified in chapter 6. The simulation is performed in chapter 7, after which it is discussed in chapter 8. The conclusions are stated in chapter 9.

2

Operation Description

Assessing the safety of an operation requires extensive knowledge of the specifics of the operation. The UAS surveillance operation is a concept, and not an actual operation yet, which means that there are a lot of aspects that cannot be specified fully at this early stage. The operation is aimed to go live at the time that the aforementioned U-space services offer an advanced level of automation of different steps in the drone operation, which is planned to be achieved by 2024 [SESAR JU, 2017]. To achieve the best possible description, input is gathered from conversations with Port of Rotterdam Authority design experts. After establishing the specifics of the operation, the exact scope of the safety assessment is specified.

2.1. Surveillance operation

It is desired to assist the marine surveillance vessels with eyes from the sky, helping to spot irregularities on the water, near quay walls, and on terminal sites. Some locations that need to be visited on a timely basis can be remote and therefore somewhat time consuming to visit with patrol ships. This can easily be done with UAS, as they are quicker than the marine patrol vessels. By traveling a specific air trajectory downstream over the northern harbor terminals and back over the southern river terminals, all of these locations can be visited in a single flight. By flying at the highest allowed altitude in very-low level airspace, which is 120 meters above ground level, the camera view can cover a wide enough area of the terminals. The surveillance cruise trajectory is shown in Figure 2.1.

In the case of an abnormality that is detected by automatic recognition software on-board the aircraft, it will not stay near the site to investigate further, but continue its course and communicate the irregularity to the marine surveillance vessels. The surveillance ships are scattered throughout the harbor area during their patrol, so that they are always nearby in case of a reported abnormality by the aircraft. Examples of abnormalities that can be picked up by the aerial camera and that are easily detectable by image recognition software are: berth occupation, oil spills, and loss of separation of marine traffic. The aircraft are controlled by onboard automatic flight control equipment, rather than ground pilots controlling the aircraft through a remote connection. It can also take-off and land autonomously. Furthermore, the current

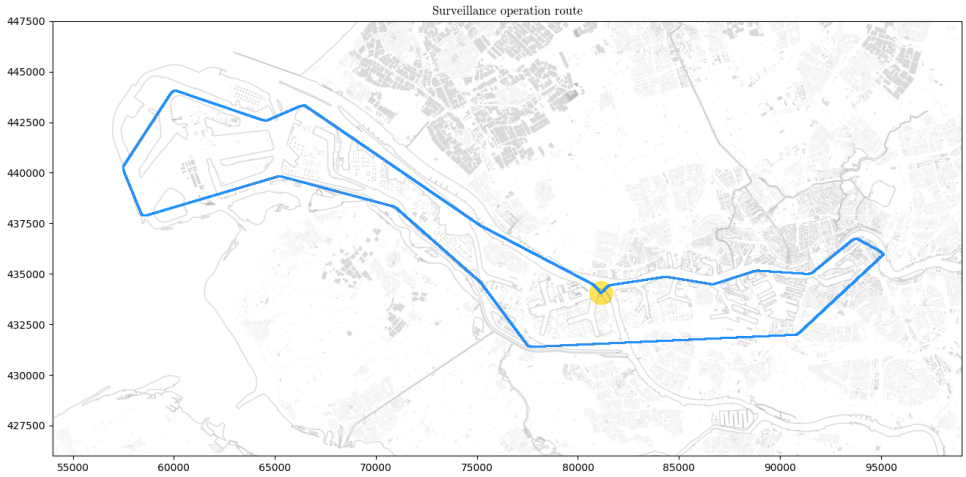

Figure 2.1: Representation of the planned trajectory of the surveillance operation. Aerodrome shown in yellow, trajectory shown in blue.

sea vessel based surveillance operation is a continuous operation, patrolling day and night. The airborne surveillance is expected to assist in this continuous day and night operation.

2.2. Flight profile

The surveillance operation follows a trajectory across the entire port area that is about a hundred kilometers in distance, as the length of the river that is covered by Port of Rotterdam Authority owned terminals stretches more than forty kilometers. Since multirotor aircraft are not as energy efficient as fixed-wing aircraft to cover such distances, a fixed-wing configuration is used for this operation. There are no abundant take-off and landing areas to accommodate the landing of fixed-wing drones, therefore vertical take-off and landing are preferred, as these can be performed in confined areas. To be able to cruise along the trajectory in fixed-wing configuration, and take-off and land in a vertical flight configuration, the aircraft is a vertical take-off and landing (VTOL) aircraft, which has a hybrid configuration with vertical thrust rotors for vertical take-off and landing, and a horizontal thrust propeller and airfoil for horizontal flight. A visual representation of this VTOL configuration can be seen in Figure 2.2.

The aircraft takes off and lands at the same location from a small take-off and landing area located in the center of the Rotterdam harbor, shown in Figure 2.1. During take-off the aircraft flies upwards in its vertical configuration, using its four vertical thrust rotors. When cleared of obstacles and the wind turbulence at low altitude that are created by these obstacles, at an altitude of 20 meters, the aircraft starts its horizontal thrust engine. When the horizontal speed is sufficient for the wings of the aircraft to gain lift, the vertical thrust rotors are switched off. The climb towards the cruise altitude of 120 meters is completed in this fixed wing configuration. The descend and deceleration also occurs in fixed wing configuration up to the altitude of 20 meters. after which the

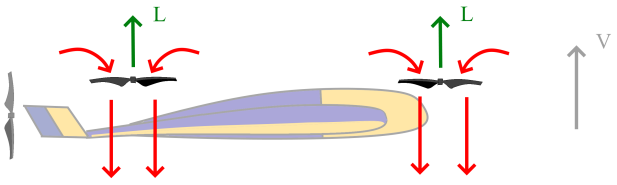

(a) Vertical configuration with lift generated by vertical rotor blades, similar to a conventional multirotor drone.

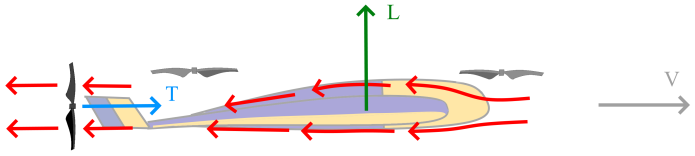

(b) Horizontal configuration with thrust generated by the horizontal propeller, and lift being generated by the airfoil.

Figure 2.2: Vertical take-off and landing configurations.

vertical thrust rotors are activated again, and the landing is performed. A graphical representation of the various stages is shown in Figure 2.3.

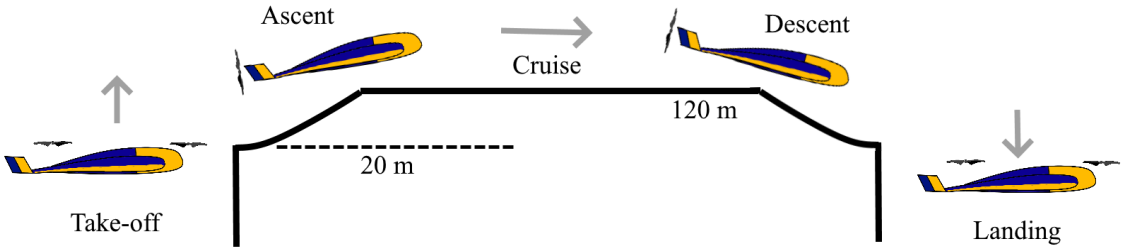

Figure 2.3: Flight profile of the different stages of the VTOL aircraft.

2.3. UAS characteristics

The aircraft chosen for this operation has a wingspan of 2.4 meters, a length of 1.3 meters, and has a maximum take-off weight (MTOW) of 12 kg. The aircraft can maintain a speed of 100 km/h for a duration of 60 minutes, which is just enough to travel along the entire 40 km harbor area downstream and back on one battery charge. As it is desired to survey each area every twenty minutes, three aircraft are used, launched twenty minutes apart from each other. The aircraft communicate each other's position to ensure a separation of about thirty kilometers along the trajectory. At the take-off and landing area a period of charging is required, therefore more than three aircraft must be fit for operation to maintain a simultaneous air coverage of three aircraft.

2.4. Level of autonomy

Flight procedures are performed without the assistance of a human pilot. The aircraft will follow the flight trajectory and avoid objects with the help of automatic flight control software. The operation is supervised by ground pilots in case of required emergency intervention. In such an emergency, the aircraft can be piloted from a

remote ground station, allowing the ground pilot to control the aircraft from a range that is beyond visual line of sight (BVLOS). Ground operators are needed to prepare the next aircraft for take-off, to remove the aircraft from the landing pad and to connect the aircraft to the charging station.

3

Relevant Literature

In this chapter, the previous research is listed, on which this research is based.

3.1. Hazard identification

To assess the safety level of an operation, all aspects that could have an influence on the level of safety must be identified. This is a challenging task as there is always a possibility of an occurrence of a hazard that has never been thought of. Several hazards accompanying UAS operations have been identified in previous literature. In Table 3.1 a list is shown of hazard causes, as identified by [Barr et al., 2017]

3.2. Scenarios resulting from possible hazards

The mentioned hazards can lead to different hazardous scenarios. [Bertrand et al., 2017] describe how different hazards lead to scenarios that are relevant for a ground risk safety assessment. Different scenarios are dependent on a conditional probability that other events occur. This relationship can be displayed in a graphical representation that is called a 'fault tree', of which an example is given in Appendix A.

[Bertrand et al., 2017] state: "Since engine failure is considered as the main source of loss of control, it is assumed that the maximum range that the vehicle can reach from the time of failure to the time of ground impact is defined by its glide range". [La Cour-Harbo, 2017] expands on this scenario by assuming that two other events can result from a loss of control, that lead to the aircraft not being able to find a safe impact zone, and describes the following 3 scenarios:

1. **Ballistic descent** The ballistic descent is a case of descent where the aircraft loses its ability to generate lift. In the case of a multirotor UAS this happens when the power supply to the rotor blades is lost, or when the rotor blades malfunction for some other reason, for example when a structural failure of the blades occurs. For a fixed wing UAS, a loss of power supply does not mean that lift generation is entirely lost. A fixed wing aircraft will only show a ballistic trajectory when the entire airfoil is unable to generate lift, in the case of a stall or structural damage.

2. **Uncontrolled glide** An uncontrolled glide occurs in a fixed wing configuration UAS when propulsion and the ability of the aircraft to maneuver are lost. The

Hazard causes
Vehicle Failures / Impairment
Control System Failures / Malfunctions / Inadequacy
Propulsion System Failure / Malfunction
Weather (Includes Rain, Snow / Icing, Thunderstorms, etc.)
Wind / Wind Shear / Turbulence (Includes Boundary Layer Effects)
Vehicle Upset Condition / Damage
Pilot Error
Power Loss / Fuel Exhaustion
Electromagnetic Interference (EMI)
Unsuccessful Launch
Flight Control System Design / Validation Errors / Inadequacy
Flight Control System Software Implementation / Verification Error / Inadequacy
Bird Strike
Payload / CG Shift / Instability
Unexpected Obstacle Encounter Results in Unstable / Aggressive Avoidance Maneuver
Boundary Layer Wind Effect
Susceptibility of Flight Control System to Key LOC Hazards (Including Failures, Wind / Weather, etc.)
Vehicle Damage (e.g., Lightning strike, damage from explosion / fire during emergency response, etc.)
Harsh Environmental Conditions (e.g., Extreme temperatures, etc.)
Cascading Factors Involving Multi-UAS Operations

Table 3.1: List of possible hazard causes, identified by [Barr et al., 2017]

aircraft is not able to steer to a safe ditching site, as opposed to the case of a controlled glide. Without the ability to manipulate control surfaces, the aircraft follows a glide path based on control surface positions according to its last trimmed state right before the occurrence of the failure.

3. **Fly-away** A fly-away happens when control is lost, but propulsion is intact. In theory, the aircraft could remain airborne until its power supply is depleted.

3.3. TPR indicators

Various indicators can be used to express the risk that accompanies a specific operation. Varying research objectives may desire different ways of indicating risk. This influences the method of calculation, and the selection of a matching indicator of the regulatory safety target. Sometimes one could be interested in the added risk of a novel operation, to research how much this adds to the risk for the general population. At other times one could want to investigate the intrinsic risk that an individual is exposed to if he was to reside at a certain location.

In literature three risk indicators are distinguished: individual, collective, and societal risk. According to [Bottelberghs, 2000], "*individual risk for a point location around a hazardous activity is defined as the probability that an average unprotected person permanently present at that point location, would get killed due to an accident at the hazardous activity.*" He defines societal risk as "*the probability that a group of more than N persons would get killed due to an accident at the hazardous activity.*" Collective risk is described by [Smets, 1996] as the expected number of third party fatalities in a given area due to the direct consequences of aircraft flight accidents during a given annum.

3.4. TPR indicator for UAS

A mathematical formulation of the individual and collective TPR risk of UAS has been defined by [Blom et al., 2020]. They define individual risk $R_I^{UAS}(y)$ due to possible crashes to the ground by a UAS operation involving multiple flights per annum as: "*The probability that an average unprotected person, who resides permanently at ground location y, would get killed due to the direct consequences of a ground crash by a UA flight during a given annum.* Collective risk R_{Cground}^{UAS} is defined as "*The expected number of third party fatalities on the ground in a given area Y due to the direct consequences of ground crashes by UA flights during a given annum*".

As identified by [Blom et al., 2020], third party risk for UAS operations had focused on the expected number of fatalities due to the i^{th} UA flight colliding with the ground $E[n_{F,i}^{UAS}]$ and is characterized as:

$$E\{n_{F,i}^{UAS}\} = \int_Y P(y, F \mid i)[1 - P(S \mid y, i)]\rho(y)dy \tag{3.1}$$

(Equation (2.6) from [Blom et al., 2020] shown here as Equation (3.1)) where $P(y, F \mid i)$ is *"The probability that an unprotected average person who is at ground location y is killed or fatally injured due to a ground crash of the i^{th} UA flight"*, $P(S \mid y, i)$ is the probability that a person at location s is sheltered against a crash of the i^{th} UA flight, $\rho(y)$ is the population density as a function of location y, and Y is the area considered.

$P(y, F \mid i)$ is characterized in UAS literature by Equation (2.7) from [Blom et al., 2020], shown in this report as Equation (3.2):

$$P(y, F \mid i) = \sum_{e \in E} \left[P(e \mid i) p_s(y \mid i, e) |A(i, e)| P(F \mid y \in A(i, e)) \right] \tag{3.2}$$

where E is the set of possible crash event types, $P(e|i)$, is the probability that the i^{th} UA flight crashes to the ground due to event type e, $p_s(y \mid i, e)$ is the probability density function of the crash location of the i^{th} UA flight under event type e, $|A(i, e)|$ denotes the size of the crash impact area $A(i, e)$, $P(F|y \in A(i, e))$ is short for $P(F \mid y \in A(i, e), i, e)$, which is the probability that the crash of the i^{th} UA flight due to event type e is fatal for an unprotected average person in the crash impact area.

3.5. Previous literature on subprobabilities

The factors that make up these equations have been researched in literature extensively, of which some relevant literature is summarized below.

Probability of an uncontrolled descent event Several studies have been done to research the level of system reliability for unmanned aircraft systems. Based on a level of complexity of the aircraft, and the severity of a the consequence of a failure, several component reliability values have been proposed, dividing components into primary and secondary systems, being systems that provide the "function installed to provide the most pertinent controls", and "redundant systems that provide this function

No safety effect	Failure conditions that would have no effect on safety.
Minor	Failure conditions that would not significantly reduce UAS safety that may include a slight reduction in safety margins or functional capabilities.
Major	Failure conditions that would reduce the capability of the UAS to cope with adverse operating conditions to the extent that there would be a significant reduction in safety margins.
Hazardous	Failure conditions that would reduce the capability of the UAS to cope with adverse operating conditions to the extent that there would be a loss of the UAS where it can be reasonably expected that a fatality will not occur, or a large reduction in safety margins or functional capabilities.
Catastrophic	Failure conditions that could result in one or more fatalities

Table 3.2: Categories of failure conditions as specified by [JARUS, 2017].

as a backup", respectively [JARUS, 2015]. This scoping paper suggests component failure probability requirements for complex light unmanned aircraft systems, which are UAS that can fly autonomously but can be taken over by a pilot in an emergency. Component failure probabilities are specified for conditions that result in different categories of outcomes, which are listed in Table 3.2. For complex systems, of which its failure could lead to a catastrophic outcome, the proposed probability of failure requirement is to be less than $1*10^{-6}$ failures per flight hour [JARUS, 2015].

[Melnyk et al., 2014] also propose system failure rates required to meet a certain threshold safety level. The used threshold level is based on the current safety record for ground casualties of general aviation, coming down to a target safety level lists different target levels of safety for system failure rates based on the weight of the UA and the area over which it operates. System failure rates are found by means of simulation. In suburban areas, the system failure rate for a small UA is set to a level of $9.14 *10^{-5}$ failures per flight hour. Other simulated values are listed in Table 3.3

Group	Remote	Rural	Suburban	Urban	Metro	City center
Group 1 (Micro)	1.20×10^{0}	1.20×10^{-1}	1.50×10^{-2}	1.50×10^{-3}	6.01×10^{-3}	2.10×10^{-4}
Group 2 (Mini)	2.73×10^{-1}	2.73×10^{-2}	3.42×10^{-3}	3.42×10^{-4}	1.37×10^{-4}	4.77×10^{-5}
Group 3 (Small)	7.31×10^{-3}	7.31×10^{-4}	9.14×10^{-5}	9.14×10^{-6}	3.66×10^{-6}	1.28×10^{-6}
Group 4 (Tactical)	1.15×10^{-3}	1.15×10^{-4}	1.43×10^{-5}	1.43×10^{-6}	5.73×10^{-7}	2.00×10^{-7}
Group 5 (Medium)	3.05×10^{-4}	3.05×10^{-5}	3.81×10^{-6}	3.81×10^{-7}	1.52×10^{-7}	5.32×10^{-8}
Group 6 (Large)	4.02×10^{-5}	4.02×10^{-6}	5.03×10^{-7}	5.03×10^{-8}	2.01×10^{-8}	7.03×10^{-9}
Group 7 (Heavy)	1.61×10^{-5}	1.61×10^{-6}	2.01×10^{-7}	2.01×10^{-8}	8.04×10^{-9}	2.81×10^{-9}

Table 3.3: Maximum system failure rates (per FH) to meet ground TLS. [Melnyk et al., 2014]

Not all failures lead to a loss of control. [Primatesta et al., 2019] identify the total probability of combined hazards that could result in an uncontrolled glide, and estimates this event probability as 0.005 failures/hour. [Bertrand et al., 2017] investigate the ground risk of a UAS mission with similar characteristics as the operation of this research, a fixed wing low altitude flight of an autonomous fixed wing aircraft to inspect railway tracks. This research uses a total probability of a loss of control of the UAS of $1*10^{-3}$ losses per hour. [Petritoli et al., 2018] compares commercial and military reliability on component level as shown in Table 3.4.

Commercial Drone (a)			
System Description	**λ_P System FIT (F/10^6 hrs)**	**MTBF (hours)**	**Incidence (%)**
Ground Control System	2.00	500,000.0	6.62%
Mainframe	2.77	360,984.8	9.16%
Power plant	9.94	100,603.6	32.88%
Navigation system	9.41	106,269.9	31.13%
Electronic system	5.01	199,600.8	16.57%
Payload	1.10	909,090.9	3.64%
λ TOTAL =	**30.23**	**FIT**	
MTBF (R_{Total}) =	**33,079.50**	**Hours**	
	1378.31	**Days**	
	49.23	**Months**	

Table 3.4: Table as illustrated by [Petritoli et al., 2018], showing total and component reliability levels for a commercial drone [military drone is left out].

Probability of a crash Failures of unmanned aircraft systems, and their resulting failure trajectories are of various nature, as described above. These trajectories have different influences on the probability that a crash happens at a certain location. In a ballistic descent the crash areas will be more close to the flight path, an uncontrolled glide can glide a bit further from the flight path, and a fly away event can be located very far away from the flight path, in theory as far as the energy storage on board the UA allows it to fly. The location of impact given an uncontrolled glide has been studied by [Bertrand et al., 2017].

Probability of fatality The probability of fatality, given an impact at a certain ground area, is performed in literature with a single approximation, or with intermediate steps of first calculating the probability of a presence of a person, given ground impact, and calculating the probability of fatality, given collision with a present person. To research the probability of a collision with a person, given a ground impact at a specific location, the probability of a person being present in the glide path is determined. Different estimations of the number of persons being present at ground locations are used in literature. [La Cour-Harbo, 2017] estimates and average number of persons per household, and plots all these households on a density map. [Grimme, 2019] uses openly available population and neighborhood geometry data to estimate person presence probability.

As identified by [Washington et al., 2017], most studies use Abbreviated Injury Scale (AIS) models to estimate a probability of fatality based on the kinetic energy of a collision with a person, or a kinetic energy level threshold which must have had a fatal consequence.

The probability of impact of a person and the probability of fatality is combined by [Range Commanders Council, 2001], by first specifying a zone along the flight path where an impact with a person would be lethal. This zone is spanned by the wingspan

of the aircraft, and a horizontal distance along the part of the glide path where it flies low enough to hit a person. The potentially lethal distance is shown in Figure 3.1, based on a graphical representation of a similar representation of a lethal area of [Lum et al., 2011].

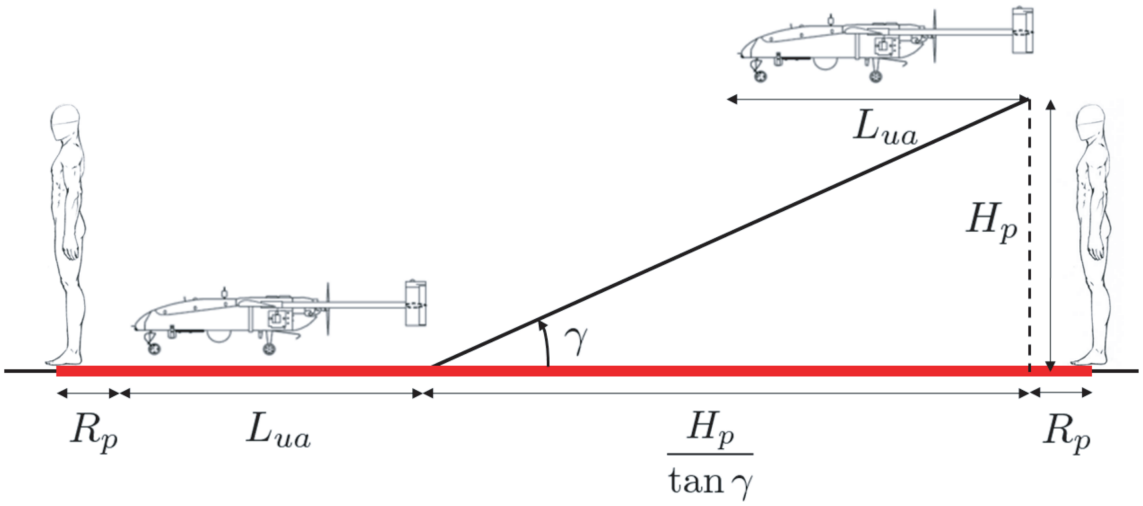

Figure 3.1: Figure as illustrated by [Lum et al., 2011], showing a potentially lethal distance during the descent of the UAS in red.

The formula for the potentially lethal area as determined by [Range Commanders Council, 2001] is given by :

$$A_{L_{Hp}} = \left(w_{ua} + 2R_p\right)\left(L_{ua} + \frac{H_p}{\tan\gamma} + 2R_p\right) \tag{3.3}$$

where w_{ua} is the wingspan of the UAS, R_p is the average radius of a person, L_{ua} is the length of the UAS, H_p is the average height of a person, and γ is the glide slope of the descent. This lethal area is used in the following formula to obtain a probability of fatality:

$$\tilde{F}_{fat} = A_{L_{Hp}} \rho_p (1 - D) \tag{3.4}$$

where ρ_p is the population density, and D is the shelter factor, i.e. the probability that a person is in a building and therefore not exposed. [Lum et al., 2011] use a protection factor of 0.5 for roads and towns, 0.1 for forests, and 0 for fields.

3.6. Influence of wind

In the calculation of the probability of an aircraft hitting the ground at a certain location, wind is an important factor. [La Cour-Harbo, 2017] specifies an uncontrolled glide to be “governed by the aircraft’s glide ratio and wind”. [Brezoescu, 2014] identified the behavior of a fixed wing UAS under the influence of wind, identifying the ‘sideslip’ technique to adjust for cross wind, where the aircraft maintains its desired heading, but rolls into the wind to correct the crosswind steering component. [Ranquist et al.,

2016] concludes that “A horizontal gust can roll the aircraft by blowing underneath one of the wings, and because banking (rolling) an aircraft changes its direction of flight, horizontal gusts are particularly dangerous”.

3.7. Target level of safety

As mentioned in chapter 1, the goal of EASA in the implementation and conduction of new operations for unmanned aircraft systems is to ensure that the safety level of manned aviation is maintained. An actual quantification has not been specified by the competent authority for UAS regulation in The Netherlands, Human Environment and Transport Inspectorate (ILT), nor by the guideline framework published by EASA. For commercial aviation, EASA mandates that the probability of a serious accident of a large manned aircraft involving injuries and/or fatalities, categorized as hazardous, must not be greater than one per ten million flight hours, equivalent to $1*10^{-7}$ fatalities per hazard per flight hour [JARUS, 2015]. To determine which accident frequency is considered safe enough for third parties, there exists a challenge in comparing accident consequences of unmanned crash impacts to those of manned crash impacts, due to the nature of the aircraft in terms of weight and size. As identified by [Jiang et al., 2020], no third-party fatality quantification is determined by JARUS to be used as a threshold level. [JARUS, 2017] does however propose a threshold of $1*10^{-6}$ per flight hour.

3.8. Simulation models

[Grimme, 2019] has developed a simulation model to research the third party risk of a package delivery operation over populated areas. This produces a density map of ground collision probabilities based on Monte Carlo failure simulations. Although the modeled aircraft is a multirotor drone, with different flight model characteristics, the model setup is suitable to be slightly altered for the assessment of the operation that is the subject of this thesis, which is further explained in chapter 5.

[Lum et al., 2011] do simulate a fixed wing aircraft trajectory. The failure trajectory is simulated by drawing simulation times from a uniform failure probability distribution, and the trajectory to the ground is simulated by running a numerical simulator until the aircraft reaches ground level. Control failure is simulated by freezing the control surfaces, sometimes leading to near 90 degree trajectories, representing a descent that is more ballistic in nature, rather than a glide path. The simulation method of [la Cour-Harbo, 2019] considers an uncontrolled glide, assuming the control surfaces after the failure occurrence to be “close to the neutral position”.

4

Research scope

For this thesis a trade-off is made between maintaining a wide high level scope, and being able to achieve in-depth results within a time frame suitable for a thesis. This results in an exact scope, which is further explained in this chapter. General statements and assumptions are mentioned, while more specific model scoping is explained in chapter 5.

4.1. Focus on quantification of risk

The goal of the safety assessment is to quantify the safety risk caused by the surveillance operation. By quantifying the risk of hazard events, a risk level can be estimated and decisions can me made on whether the risk levels are acceptable. This has a benefit compared to making a qualitative list of possible hazards, as a quantified risk level can be compared to a threshold value. Although the combined level of safety risk consists of a summation of the risk resulting from events that are outside of the scope of this research, it is desirable to quantify the risk of the scenario of an uncontrolled glide event, and verify that the level is below the target level of safety.

4.2. Operational scope

The operation is carried out with a VTOL aircraft, as previously explained. Only the selected aircraft is used in the assessment, instead of a comparison of different aircraft types. The vertical takeoff part of the operation only takes place between an altitude of zero and twenty meters. The vertical take-off stage is assumed not to pose ground risk and is therefore not considered in this research, and the simulation starts at an altitude of 20 meters when the VTOL aircraft has already picked up enough speed to have been fully transitioned to the fixed wing configuration. Implementing the transition process in the dynamic model is not considered to outweigh risk model accuracy, and is therefore not looked at in this thesis. Although not including the vertical flight part of the operation, still the largest section of the climb and descent are in horizontal flight mode, which are indeed considered in this thesis.

The operational time window considered in the safety assessment is a time window where most of the population working in the seaport area has finished their morning commute, leading to an increased population density in the industrial areas. As the

flight path of the operation mainly covers industrial areas, it is estimated that this will result in the most conservative risk level. The considered time window ends before the commute back to residential areas. Note that, as described in section 2.1, the operation extends beyond this time frame.

4.3. Considered hazards and events

Several aspects of the operation can add to an increased safety risk. As can be seen in the example event tree of Appendix A, multiple hazards and events can lead to contact with the ground at a time and place that is not in the flight plan. The displayed events have different probabilities of occurring, which can not all be addressed for the scope of this thesis. The less suitable scenarios to be selected as the subject for this thesis are explained below, after which the scenario that is considered to be the most valuable to research is mentioned in the end of this section.

The scenario of a ballistic descent has different hazard causes for a fixed wing UA, compared to the multirotor UAS operation on which [Grimme, 2019] assessed a ballistic descent. This is because multirotors do not have an airfoil to create lift when the vertical thrust system fails. Fixed wing UAS are capable of ending up in a ballistic descent, however mainly due to events such as a structural failure, or a mid-air collision, which are not considered to be the most valuable aspects to start the assessment with. A ground impact location resulting from a fly away event is difficult to simulate, and therefore more difficult to quantify, as this takes a completely different stochastic modeling approach. A controlled glide event and the emergency vertical landing event differ from each other in the case of separate a horizontal thrust failure, where the VTOL aircraft can switch to the vertical flight configuration and land at a suitable spot. If the vertical thrust would become unavailable at the same time, the aircraft could use its vertical configuration to glide and steer to a ditch location. The automatic emergency landing software installed in most latest UAS that are capable of autonomous flight are able to choose a less vulnerable ground area to ditch into. Hazards resulting from malicious intent are not considered, as this would lean towards a security risk assessment, and this thesis focuses on assessing safety risk.

This thesis focuses on the hazard of a complete power failure, resulting in the loss of power and control, and the consequent event scenario of and uncontrolled glide into the ground risk of the operation.

4.4. Air risk

The aircraft is assumed to operate in a confined space, a so called ‘geofence’, that no other aircraft may enter. Accidental trajectory incursions are not considered for this thesis (neither manned or unmanned), and therefore the interaction or possible intervention of an air traffic control system is also not taken into account. Possibly resulting mid-air collisions, which are potential hazard causes for drone operations, are not considered in this research. Other scenarios, however, such as a fly away and uncontrolled glide, can result in the aircraft leaving its geofence volume, and ending up in airspace where other aircraft are flying. Increased air risk resulting from reduced separation with cooperating drones from the same surveillance operation is not

researched in this thesis, as the aircraft are spaced more than ten kilometers apart while following the operation trajectory. Leaving out the air risk means that this research focuses on the ground risk

4.5. Assumptions on wind behavior

Wind is a major hazard for unmanned aircraft systems, as “wind and turbulence play the largest role in aviation weather accidents”. For small UAS, “ways in which wind affects sUAS include changing the flight trajectory, limiting control, and reducing endurance (e.g. battery life)”. [Ranquist et al., 2016]. Although wind is a hazard that has a big influence on the added safety risk of third parties on the ground, it is assumed that tactical measures are taken, that do not allow the aircraft to fly when wind conditions could lead to a loss of control, or to an increased flight time that will deplete the battery. Furthermore, it is assumed that worsening wind conditions are detected in advance so that the aircraft will not encounter these conditions during flight, which would make it impossible to land.

The influence of wind is often modeled from a symmetric probability distribution, accounting for variance in average wind speed, which make up the gusts. For this specific coastal operation, with the Rotterdam harbor having stronger than average winds [KNMI, 2020], it is desired to investigate the influence of these specific wind conditions on the ground impact distribution. Wind can be modeled with the help the Dryden gust model. This model allows for simulation of the magnitude and rotation of gusts in all three directions and around all three body axes. For this research, only the two horizontal directions are considered. Vertical direction of wind gust and rotation around the vertical axis are assumed to be zero.

5

Model Description

The model setup that is used as a method to assess the safety risk in this thesis is described in this chapter. The high level model framework of [Blom et al., 2020] is used as a backbone, and similar to how this model is applied to the operation of a parcel delivery operation of [Grimme, 2019], the used application for this thesis is described below. Because in this model a multirotor aircraft is used, the fixed wing aircraft equations of motion for this thesis are taken from Brezoescu [2014]. The first section describes the steps of the widely applicable TPR model how it is described by [Blom et al., 2020]. The used steps are quoted and displayed with *italics*, using remarks where a different approach is used for this thesis. Elaborate approaches are explained separately in the following sections.

Third party risk for UAS operations is generally expressed as the number of fatalities due to the i^{th} UA flight colliding with the ground $n_{F,i}^{UAS}$. The expected number of fatalities due to the i^{th} UA flight colliding with the ground '$E\{n_{F,i}^{UAS}\}$' , is derived from literature by [Blom et al., 2020] and characterized as:

$$E\{n_{F,i}^{UAS}\} = \int_Y P(y, F \mid i)[1 - P(S \mid y, i)]\rho(y)dy \tag{5.1}$$

(Equation (2.6) from [Blom et al., 2020] shown here as Equation (5.1)) where $P(y, F \mid i)$ is *"The probability that an unprotected average person who is at ground location y is killed or fatally injured due to a ground crash of the i^{th} UA flight"*, $P(S \mid y, i)$ is the probability that a person at location s is sheltered against a crash of the i^{th} UA flight, $\rho(y)$ is the population density as a function of location y, and Y is the area considered.

The Collective ground risk of the i^{th} flight equals the expected number of fatalities due to the i^{th} UA flight colliding with the ground, $R_{\text{Cground}}^{i} = E\{n_{F,i}^{UAS}\}$, and substituting Equation (5.1) into this, results in the following equation for R_{Cground}^{i}: (Equation (3.3) from [Blom et al., 2020], shown here as Equation (5.2))

$$R_{\text{Cground}}^{i} = \int_Y P(y, F \mid i)[1 - P(S \mid y, i)]\rho(y)dy \tag{5.2}$$

$P(y,F \mid i)$ is characterized in UAS literature by Equation (2.7) from [Blom et al., 2020], shown in this report as Equation (5.3):

$$P(y,F \mid i) = \sum_{e \in E} \left[P(e \mid i) p_s(y \mid i,e) |A(i,e)| P(F \mid y \in A(i,e)) \right] \tag{5.3}$$

where E is the set of possible crash event types, $P(e|i)$, is the probability that the i^{th} UA flight crashes to the ground due to event type e, $p_s(y \mid i,e)$ is the probability density function of the crash location of the i^{th} UA flight under event type e, $|A(i,e)|$ denotes the size of the crash impact area $A(i,e)$, $P(F|y \in A(i,e))$ is short for $P(F \mid y \in A(i,e),i,e)$, which is the probability that the crash of the i^{th} UA flight due to event type e is fatal for an unprotected average person in the crash impact area.

For this thesis, the steps are used that lead to the risk per flight hour, which is the Collective ground risk per flight R^i_{Cground}, divided by the the nominal duration of the i^{th} flight.

5.1. Evaluation steps

The step wise model framework considers a UAS based operation conducting N flight per annum over an area Y, using different types of UAs. The volume of airspace used by these N flights is separated from airspace in use by Commercial Air Transport, General Aviation and Urban Air Mobility operations.

Step 1: *Simulation of N nominal flight paths. Generate for each of the N flights, i.e. $i = 1,\ldots,N$, the UA type $d_i \in D$, the route points, the nominal four-dimensional flight path and the nominal duration T_i^{nom}.*

Remark: The three-dimensional nominal flight path is obtained by determining the three-dimensional route points as described in this step. However, generating a four-dimensional trajectory is done based on an average nominal wind vector $w_{t_{nom}}$, corrected for geographic position and altitude. This nominal wind vector is more extensively described in section 5.2.

Step 2: *Evaluate the probability of crash. Calculate for each of the N flights and each $e \in E$ the probability of crash:*

$$P(e \mid i) = 1 - \exp\left(-\lambda_{i,e} T_i^{nom}\right) \tag{5.4}$$

with $\lambda_{i,e}$ the rate of event e to happen during the i^{th} flight. Typically the i-dependency of $\lambda_{i,e}$ concerns the type of UA d_i.

Step 3: *Simulation of UA flights that crash. Conduct for each of the N flights and each $e \in E$ a Monte Carlo simulation consisting of K_i^e runs, i.e. for $k = 1, \ldots, K_i^e$ with*

$$K_i^e = \text{Entier}(T_i^{nom}) \tag{5.5}$$

Remark: In this thesis K_i^e = 500000 is used, because only one flight that has a T_i^{nom} of 3200 seconds is assessed.

Each of these MC runs involves the following three substeps:

Substep 3.1: *Generate the random moment of event time $t_e^{i,k} \sim U\left(0, T_i^{nom}\right)$ for $k = 1, \ldots, K_i^e$, $e \in E$.*

Substep 3.2: *Simulate for the i,k-th flight the UA state at moment of failure event $t_e^{i,k}$. The UA state components to be generated are 3D position $s_{t_e}^{i,k}$, 3D velocity $v_{t_e}^{i,k}$ and attitude $\theta_{t_e}^{i,k}$:*

$$\begin{aligned} s_{t_e}^{i,k} &= s_{t_e}^{i,nom} + \varepsilon_{te}^S \\ v_{t_e}^{i,k} &= v_{t_e}^{i,nom} \\ \theta_{t_e}^{i,k} &= \theta_{t_e}^{i,nom} \end{aligned} \tag{5.6}$$

where $(s_{t_e}^{i,k}, v_{t_e}^{i,k}, \theta_{t_e}^{i,k})$ are the nominal state components from the i^{th} nominal flight plan, and (ε_{te}^S) is the Gaussian navigation error in horizontal and vertical position with standard deviations $\left(\sigma_H^s, \sigma_V^S\right)$. Typically UA navigation is based on Global Positioning System, for which $\left(\sigma_H^s, \sigma_V^S\right)$ values have been standardized [Department Of Defense, 2008].

Remark: In this thesis, the GPS error is assumed to be absent, and the deviation from the nominal flight path ε_{te}^S is obtained by running the dynamic flight model under the influence of randomly generated wind turbulence. The used flight model in based on the description in the next step, and adjusted for a fixed wing aircraft. Furthermore, course manipulation controls are added. The altered model and the wind turbulence generation are further described in section 5.3.

Substep 3.3: *Simulate the i,k-th flight on the time interval $\left[t_e^{i,k}, t_{c,e}^{i,k}\right]$, i.e. from $t_e^{i,k}$ until moment of ground crash $t_{c,e}^{i,k}$; this yields the UA state $x_{c,e}^{i,k}$, at moment $t_{c,e}^{i,k}$. The applicable differential equations to be used depend of the event type e and the desired model fidelity. As an example we provide the differential equations from [Cour-Harbo, 2020] for a ballistic descent model of a quadcopter under full thrust loss:*

$$\begin{aligned} \dot{s}_t &= v_t \\ \dot{v}_t &= a_t \\ a_t &= \mathrm{Col}\{0,0,g\} - C_D A_S \varrho_t \| v_t - w_t \| (v_t - w_t)/2m \end{aligned} \tag{5.7}$$

where g is the gravitational constant, C_D is the drag coefficient, A_S the surface area, m is the mass of the UA + payload, ϱ_t and w_t are air density and wind velocity vector at moment t, respectively. The latter two are considered to be functions of 3 dimensional position s_t. Rather than adding the wind effect in the differential equation for the position as is done in [Cunningham et al., 2016], w_t is incorporated in the drag component of the acceleration [Grimme, 2019]

Remark: w_t generation during uncontrolled glide is simulated using the dynamic flight model of substep 3.2. Thrust and steering forces are considered zero, $S_{c,t} = 0$, $T_t = 0$. Mass is considered fixed, and a payload is considered absent.

Step 4: *Estimating the probability density to hit a location in grid cells in Y. Calculate for each grid cell G_j in Y, and for each $e \in E$ and each $i = 1, \ldots, N$, the estimated probability:*

$$\hat{P}(j \mid i, e) = \sum_{k=1}^{K_i^e} \left[1[\mathbf{s}_{c,e}^{i,k} \in G_j] \right] / K_i^e \tag{5.8}$$

where $\mathbf{s}_{c,e}^{i,k}$ is the simulated UA position at crash moment $t_{c,e}^{i,k}$, and 1 is an indicator function, i.e. 1[true] = 1, 1[false] = 0. Subsequently the estimated local density is calculated for an arbitrary location y_j in grid cell G_j and for each $e \in E$ and each $i = 1, \ldots, N$:

$$\hat{p}_s\left(y_j \mid i, e\right) = \hat{P}\left(j \mid i, e\right) / \left|G_j\right| \tag{5.9}$$

where $\left|G_j\right|$ is the area size of the j^{th} grid cell. K should be such large that there are sufficient counts per grid cell; hence the smaller $\left|G_j\right|$, the larger K.

Step 5: *Estimating the probability of fatality for hitting an unprotected person in each grid cell. Based on eq. (3.6) we can evaluate for each j, i, e for which $\hat{P}(j \mid i, e) > 0$, the estimator*

$$\hat{P}(F \mid j, i, e) = \hat{P}(F, j \mid i, e) / \widehat{P}(j \mid i, e) \tag{5.10}$$

with nominator

$$\hat{P}(F, j \mid i, e) = \sum_{k=1}^{K_i^e} \left[1\left[s_{c,e}^{i,k} \in G_j \right] P\left(F \mid v_{c,e}^{i,k} s_{c,e}^{i,k} \in A(i,e) \right) \right] / K_i^e \tag{5.11}$$

Step 6: *Estimate Individual risk per UA flight for each grid cell of Y. Based on equation (2.7)* [In this thesis: Equation (5.3)] *the estimator of individual risk for an arbitrary location y_j in grid cell G_j due to the i^{th} flight yields:*

$$\hat{P}\left(y_j, F \mid i\right) = \sum_{e \in E} \left[P(e \mid i)\, \hat{p}_s\left(y_j \mid i, e\right) |A(i,e)| \hat{P}(F \mid j, i, e) \right] \tag{5.12}$$

Remark: Step 7 and 8 are skipped, as these steps of the high level model framework are not relevant for the scope of this thesis.

Step 9: *Assess the population map $\hat{\rho}_j = \rho\left(y_j\right)\left|G_j\right|$ for each grid cell G_j*

Remark: Population assessment based on building density is described in section 5.4.

Step 10: *Assess for each grid cell G_j the probability of shelter protection against a ground crash of the i^{th} UA flight. This yield estimated shelter probability $\hat{P}(S \mid j, i)$ for each j, i.*

Step 11: *Estimate Collective ground risk per flight. Calculate the estimated Collective ground risk per UA flight in area Y using eq. (3.3):*

$$\hat{R}^i_{\text{Cground}} = \sum_j \left[\hat{P}\left(y_j, F \mid i\right) [1 - \hat{P}(S \mid j, i)] \hat{\rho}_j \right] \tag{5.13}$$

Step 12: *Estimate Collective ground risk per flight hour for each flight. Calculate, for each i, the collective ground risk per UA flight hour:*

$$\hat{R}^i_{\text{Cground}} / T_i^{nom} \tag{5.14}$$

and present the results for the N annual flights as an empirical density.

Remark: For this operation, $N = 1$.

Step 13: *Verify if a part of this empirical density passes an applicable threshold level. For example, [JARUS, 2017] proposed a threshold of 10^{-6} fatal injuries on the ground per UA flight hour. For the part above the threshold it has to be evaluated what this means for the UAS operation considered.*

5.2. Nominal flight path

The three-dimensional nominal flight path is obtained by determining the waypoints that form the nominal flight path, as described in step 1. The four-dimensional nominal flight path is determined by calculating the position of the aircraft in between the consecutive waypoints, based on nominal flight model inputs. The nominal flight is simulated under one wind condition, the average wind vector based on KNMI data measured over the year 2019.

Obtaining the nominal wind vector The 'average wind vector' has different methods of approximation. The method of [Grange, 2014] is applied. Representative wind data must be acquired to use as a model input. Measured data near a measuring station does not equal the wind vector data around the aircraft, and must therefore be adjusted for geographical position and altitude.

Correcting for geographical position Two measuring stations located on opposite ends of the trajectory of the surveillance operation are used to approximate the wind vector at ground level at a geographical location at some point on the flight trajectory. Wind magnitude depends on the distance to the coast line, as winds are stronger near coastal areas compared to inland areas. The flight trajectory has a somewhat stretched shape, resulting in each location directly under the flight trajectory being roughly near an imaginary line that is perpendicular to the coast line. The coast line of the coastal area of South-Holland is also approximated as a line, for the 'coastal distance' approximation line to be perpendicular to the coast line, as shown in Figure 5.1.

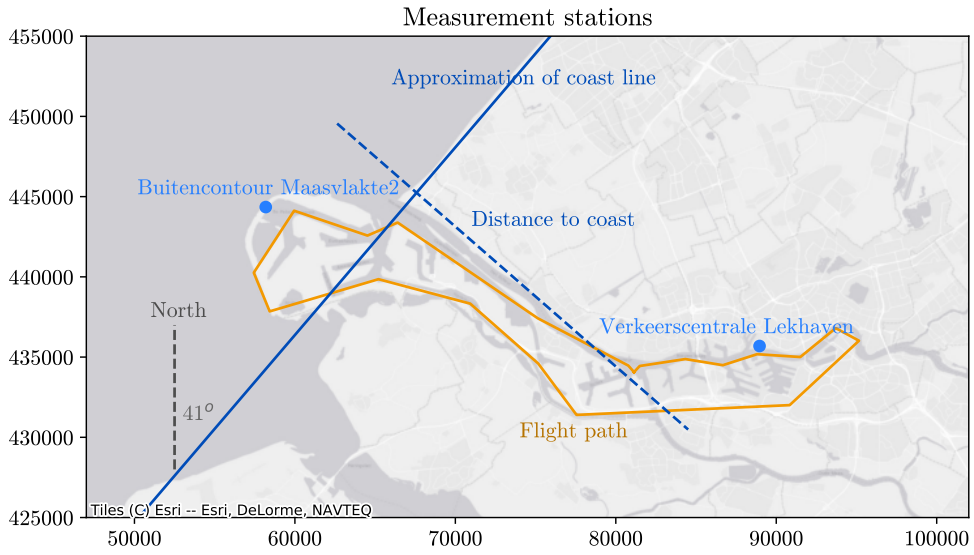

Figure 5.1: Measuring station located near the coast and inland are used as an estimate of wind strength as a function of the distance of a location to the linear approximation of the coast line.

The measurement data coastal distance is projected onto the line, resulting in a coastal distance of both measurement stations located on opposite ends of the 'distance to coast' line. The wind vector of a position along the flight trajectory is obtained by

projecting its coastal distance onto the line, and multiplying the distance with the wind vector gradient along the coastal distance line. The approximated distance of a point to the coast is obtained by expressing the location of the point in a reference frame rotated 41 degrees around the vertical axis. 41 degrees is the angle that the approximated coast line makes with the northern axis, as is indicated. An approximation of the wind vector at ground speed can be found by using the formula:

$$w_t(y'_j) = \frac{w_{t,inland} - w_{t,coastal}}{y'_{coastal}} * y'_j + w_{t,coastal} \tag{5.15}$$

where $w_t(y'_j)$,$w_{t,coastal}$, and $w_{t,inland}$ are the wind velocity vectors near the ground for some location y_j, the coastal station, and inland station respectively. y'_j and $y'_{coastal}$ are the coastal distances along the 'distance to coast' line relative to the coastal station, which itself has a y' of zero.

Wind at altitude The average wind vector is used for the nominal flight simulation. Since this is measured at 6 meters above ground level, a correction for altitude needs to be made. Altitude correction is not determined in the same way that it is performed by [Grimme, 2019], as a correction for altitude is already included in the used method for turbulence generation. For the determination of the nominal flight path, turbulence is not yet taken into account. To still be able to obtain a nominal flight vector $w_{t_{nom}}$ that is corrected for altitude, the wind turbulence simulation model, which is explained in the next section, is fed with zero signal, rather than an Monte Carlo generated random signal, resulting in a zero turbulence wind vector corrected for altitude.

5.3. Generating deviation from nominal flight path

The deviation from the nominal flight path results from the effects of random wind turbulence. This deviation information is used as an initial starting position for the generated uncontrolled glide failure scenarios. The effects are determined by storing the deviation information while running the dynamic flight model, obtaining a multi-dimensional empirical distribution. The dynamic flight model for a fixed wing aircraft from [Kai et al., 2019] is used, simplified where possible to account for computation time.

Dynamic flight model The dynamic flight model is described by the differential equations of the aircraft, navigational calculations and course adjustment calculations. The aircraft is modeled as a point mass in three-dimensional space. The point mass is has fixed dynamical characteristics, such as mass, maximum thrust for propulsion and a maximum force for changing direction. The aircraft states that vary over time are shown in the aircraft's state vector are shown in Equation (5.16),

$$x_t = \begin{bmatrix} s_t \\ v_t \\ \theta_t \end{bmatrix} \tag{5.16}$$

where s_t represents the three dimensional position vector at time t, v_t represents the three dimensional velocity vector, and θ_t the three dimensional attitude unit vector. All vectors are expressed in an earth fixed coordinate system, and displayed in this report as boldface to indicate that the symbol represents a vector having three components in the inertial reference frame. The axis of this inertial reference system are aligned with the used global coordinate system: the Amersfoort / RD New projected coordinate system EPSG 28992. Because all vectors are expressed in the same reference system, the orientation of the body fixed reference frame with respect to the earth fixed reference system does not have to be include in the state vector. Because of the first argument of a coordinate is expressed positively in the eastern direction, and the second argument in the northern direction, to maintain a right handed coordinate system, the height above mean sea level (MSL) is a positive number.

The resulting differential equations that define the motion of the UA are stated in Equation (5.17),

$$\begin{array}{rcl} \dot{s}_t & = & \dot{v}_t \\ \dot{v}_t & = & a_t \\ a_t & = & \frac{Q_{c,t}+T_t+D_t+L_t+W}{m} \end{array} \tag{5.17}$$

where a_t is the aircraft's acceleration, m is the mass of the UA, and T_t, D_t, L_t, W are the thrust, drag, lift and weight vectors respectively. $Q_{c,t}$ represents the steering control vector, and is the only force in the model that can be used for dynamic control. The uncontrolled force vectors are defined by the following equations:

$$\begin{array}{l} D_t = -0.5 C_D A_S \varrho_t \| v_t - w_t \| (v_t - w_t) \\ L_t = -0.5 C_L S_S \varrho_t \| v_t - w_t \| (v_t - w_t) \\ T_t = T_{cruise} \hat{\theta}_t \\ W = Col\{0, 0, mg\} \end{array} \tag{5.18}$$

where C_D and C_L represent the drag and lift coefficient respectively, A_S represents the frontal area of the UA, S_S represents the wing area of the UA, ϱ_t represents the air density as a function of time, w_t represents the wind velocity with respect to time, T_{cruise} represents the thrust force, and g the gravitational acceleration

The assumptions with respect to the dynamic model, as listed in chapter 4 are repeated below:

1. A single steering force vector $Q_{c,t}$ is used as a control vector, which replaces the three control surface controls that manipulate pitch, roll and bank angle. The steering vector acts perpendicular to the thrust force vector.
2. Thrust is kept constant, and its magnitude is not controlled.
3. The thrust vector is assumed to act in the direction of the aircraft's attitude, and has a different value for the ascent, cruise, and descent stages, but remains constant.
4. The attitude vector always acts in the direction of the air speed vector.

5. All the force vectors are assumed to have their line of action through the center of gravity of the aircraft, so no torque acts around the center of gravity.

In this research the vertical component of the wind velocity vector w_t is assumed to be zero. For simplicity, aerodynamic moments around the center of gravity of the aircraft from forces generated by wind are taken zero. Note that changes in the wind velocity component do cause changes of the airspeed, therefore affecting the lift and drag components, which magnitudes are a function of airspeed.

Navigation calculations Part of the navigation calculations are the ability to iterate through a list of waypoints, and to calculate an adjusted flight path $h_{AP,t}$. When the aircraft reaches the waypoint that the nominal flight path vector, waypoint vector $h_{WP,t}$, is leading towards, the next waypoint is selected. When switching to the next waypoint upon reaching the waypoint, the new waypoint vector $h_{WP,t}$ is selected. When this new waypoint vector is selected upon the moment of reaching the waypoint, it is too late to smoothly line up with the next waypoint vector $h_{WP,t}$, leading to an overshoot of the flight path. To account for this, a distance from the waypoint is set, at which the next waypoint is selected. This distance creates some slack, giving the aircraft enough time and space to establish a smooth lineup with the next flight leg's flight path. The simulation of the deviation from the nominal flight path is ended as soon as the distance to the last waypoint is within the slack distance.

Maintaining the nominal flight path course is done by continuously calculating an adjusted flight path vector $\hat{h}_{AP,t}$ to remain lined up with the nominal flight path, or to pick up the nominal flight path when deviated from the nominal flight path. The adjusted flight path vector $\hat{h}_{AP,t}$ is chosen as a vector that lies in between the vector that points from the aircraft's position towards the next waypoint, indicated in Figure 5.2 as $h_{WP,t}$, and the vector that points form the aircraft's position directly onto the flight path, indicated as $h_{OP,t}$. The reason why the adjusted flight path has to lie on the plane in between vector $h_{WP,t}$ and vector $h_{OP,t}$ is as follows: If the aircraft would line up with vector $h_{WP,t}$, the deviation from the flight path is not actively reduced, it just gradually reduces as the aircraft approaches the next waypoint. By actively steering in the direction of $h_{OP,t}$, the deviation can be reduced. Steering too much into the direction of $h_{OP,t}$ can lead to the aircraft overshooting the flight path, due to angular acceleration of the aircraft being limited, increasing difficulty to compensate momentum. As the deviation from the flight path, the length of vector $h_{OP,t}$, $|h_{OP,t}|$ increases, the correction towards the flight path along vector $h_{OP,t}$ needs to be increased. As the velocity v in which this deviation reduces is increased, and therefore the risk of overshooting is increased, the flight path along vector $h_{OP,t}$ needs to be reduced. The relation in which the desired adjustment of the flight path vector $h_{AP,t}$ is calculated based on v_t, $h_{OP,t}$ and $h_{AP,t}$ is shown in Equation (5.19).

$$\begin{aligned} h_{AP,t} &= 0.1 * \hat{h}_{OP,t} * \sqrt{\frac{|h_{OP,t}|}{|v_t|}} + \hat{h}_{WP,t}, \\ \hat{h}_{AP,t} &= \frac{h_{AP,t}}{|h_{AP,t}|} \end{aligned} \tag{5.19}$$

The formula is an approximation of the method described by paragraph 3.3.2 from [Kai

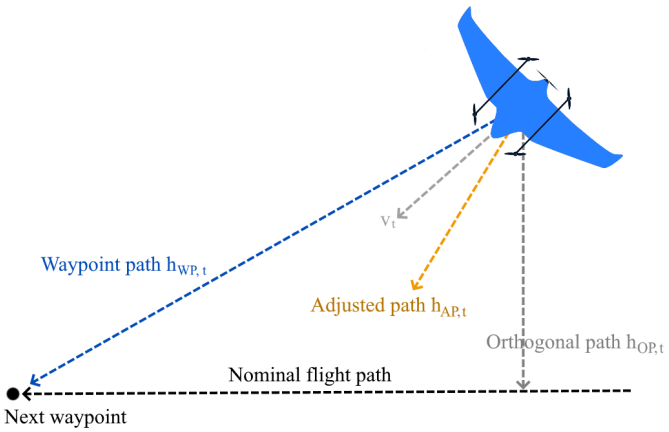

Figure 5.2: Path directions used in the formula to calculate the adjusted path.

et al., 2019] of intercepting the nominal flight path using a circular flight path. The vector $h_{AP,t}$ is continuously calculated from the changing formula inputs, which are caused by the aircraft's position and velocity. The vector $h_{AP,t}$ lines up with flight path $h_{FP,t}$ as the aircraft approaches the flight path, resulting in a smooth alignment with the flight path.

Steering control For the aircraft itself to have a smooth alignment with the flight path, its ground velocity must be aligned smoothly with the calculated flight path adjustment. In the case of a misalignment of the velocity vector v with the adjusted flight path vector $h_{AP,t}$, as shown in Figure 5.3b, a change in velocity is desired, indicated as '$\dot{v}_{t_d}$'. The desired velocity rate can be calculated from the ground velocity vector v_t and the unit vectors of $h_{AP,t}$ and v_t, $\hat{h}_{AP,t}$ and $\hat{v}_t$ respectively, as shown in Equation (5.20).

$$\dot{v}_{t_d} = \left(\left(v_t \cdot \hat{h}_{AP,t}\right) * \hat{h}_{AP,t} - \left(\left(\left(v_t \cdot \hat{h}_{AP,t}\right) * \hat{h}_{AP,t}\right) \cdot \hat{v}_t\right) * \hat{v}_t\right) * \frac{|v_t|}{|\left(\left(\left(v_t \cdot \hat{h}_{AP,t}\right) * \hat{h}_{AP,t}\right) \cdot \hat{v}_t\right) * \hat{v}_t|} \tag{5.20}$$

In order to achieve an acceleration in this direction, the sum of the forces acting on the aircraft from Equation (5.17) must act in the direction of $\dot{v}_{t,d}$. In other words, a desired steering vector $Q_{c,td}$ must be determined. This is obtained according to the formula of Equation (5.21):

$$Q_{c,t_d} = \dot{v}_{t_d} * m - (T_t + D_t + L_t + W) \tag{5.21}$$

It can be derived from Equation (5.21) that the aircraft is able to determine a Q_{c,t_d} based on the actual drag force D_t, and therefore is able to measure the wind speed that determines the drag force without error.

The aircraft's actual steering force $Q_{c,t}$ is assumed not to have a component in the direction of T_t, as this results in a forward or backward acceleration, which is not possible as the aircraft can not generate added propulsion by steering. The steering

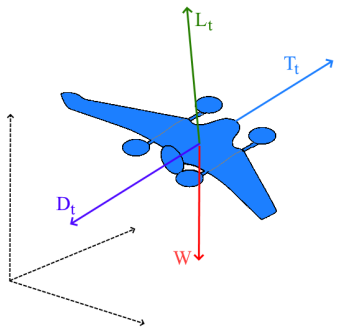

(a) Forces acting on UAS.

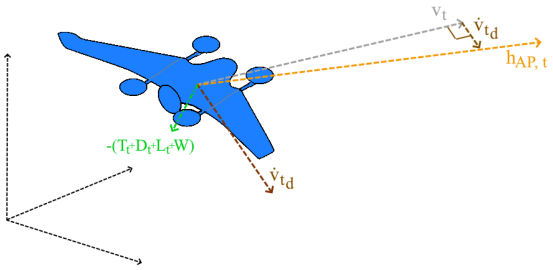

(b) Desired acceleration $\dot{v}_{t_d}$ and resultant force.

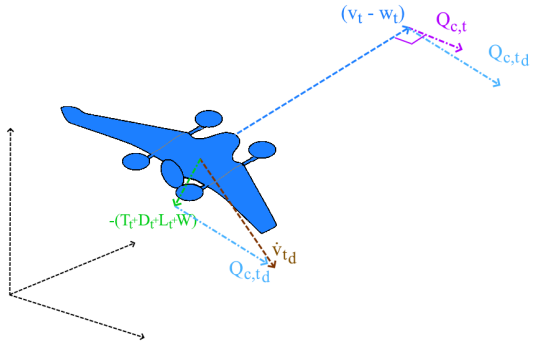

(c) Desired steering vector Q_{c,t_d}.

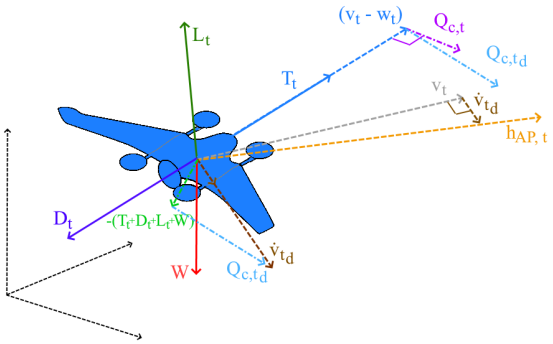

(d) All vectors.

Figure 5.3: Graphical vector representation of the model.

force $Q_{c,t}$ therefore acts perpendicular to the direction of T_t. To ensure a maximum projected component of $Q_{c,t}$ in the direction of Q_{c,t_d}, $Q_{c,t}$ lies on the plane spanned by Q_{c,t_d} and T_t. The formula of $Q_{c,t}$ is shown in Equation (5.22)

$$Q_{c,t} = \begin{cases} \frac{T_t \times \left(Q_{c,t_d} \times T_t\right)}{|T_t \times \left(Q_{c,t_d} \times T_t\right)|} * |Q_{c,t_d}| & \text{for } |Q_{c,t_d}| <= Q_{c_{max}}, \\ & \text{and} \\ \frac{T_t \times \left(Q_{c,t_d} \times T_t\right)}{|T_t \times \left(Q_{c,t_d} \times T_t\right)|} * Q_{c_{max}} & \text{for } |Q_{c,t_d}| > Q_{c_{max}}. \end{cases} \tag{5.22}$$

A graphical representation of the relation between Q_{c,t_d} and $Q_{c,t}$ is shown in Figure 5.3c.

Sampling wind turbulence To obtain turbulence time series in the air around the UAS, the approach of [Brezoescu, 2014] is adopted, in which the so called Dryden turbulence model [United States Military, 2012] is applied.

The Dryden wind turbulence model produces a turbulence value at altitude based on a wind measurement at 20 feet (6 m) above the ground, the airspeed of the vehicle, and a gust scale length and a turbulence intensity, of which the latter two are dependent of altitude. Turbulence samples are obtained by generating a random discrete white noise

signal, and filtering it with the discrete Dryden filter. The block diagram of this linear filter system is shown in Figure 5.4

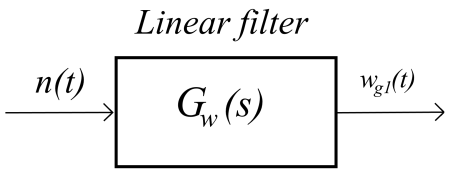

Figure 5.4: Block diagram representation of linear filter. [Stroe and Andrei, 2016]

The random discrete white noise signal is a Gaussian signal with a zero mean and a variance σ_η of one. Samples are generated with a sample period T_s, and fed to the Dryden filter, of which the z-domain transfer function is given in Equation (5.23).

$$u_{g_{(n+1)}} = \left(1 - \frac{V_a}{L_u} T_s\right) u_{g_{(n)}} + \sqrt{2 \frac{V_a}{L_u} T_s} \frac{\sigma_u}{\sigma_\eta} \eta_1 \tag{5.23}$$

V_a is given in ft/s, u_g is the turbulence magnitude (ft/s), L_u is the turbulence scale length (ft), σ_u the turbulence intensity (ft/s), and η_1 the generated white noise sample.

The formulas for L_u and σ_u are given below:

$$L_u = \frac{h}{(0.177 + 0.000823h)^{1.2}} \tag{5.24}$$

$$\sigma_u = \frac{0.1 W_{20}}{(0.177 + 0.000823h)^{0.4}} \tag{5.25}$$

where h represents the altitude of the aircraft (ft), and W_{20} is the wind velocity at 20 feet (ft/s). These last two equations are adjusted to be valid for flying at lower altitudes up to 1000 feet.

Wind measurement updates Data is stored at a resolution of Δt seconds and wind turbulence data in-between measurements is therefore estimated with the use of the Monte Carlo method.

A new turbulence sample is generated from the Dryden turbulence model, with every iteration of the aircraft model simulation, using the updated inputs of airspeed and position including altitude. This includes making a new estimate of the ground wind velocity vector based on coastal distance. An updated input from the measurements of the measuring stations is only updated every Δt seconds. This results in sudden jumps of the generated turbulence samples every Δt seconds. To account for this, the ground measurement vectors $w_{t,coastal}$ and $w_{t,inland}$ used in Equation (5.15) are assumed to change towards their updated value linearly during the Δt second interval. This results in the following equations:

$$w_{t,coastal}(t) = \frac{w_{t,coastal(t_u+\Delta t)} - w_{t,coastal\,t_u}}{\Delta t} * (t - t_u) + w_{t,coastal\,t_u} \tag{5.26}$$

$$w_{t,inland}(t) = \frac{w_{t,inland(t_u+\Delta t)} - w_{t,inland\,t_u}}{\Delta t} * (t - t_u) + w_{t,inland\,t_u} \tag{5.27}$$

t_u represents the time of the latest update from the wind measurements, $w_{t,coastal\,t_u}$ represents the wind vector measurement update taken at time t_u, and $w_{t,coastal(t_u+\Delta t)}$ represents the next wind vector measurement, Δt seconds after t_u. For a better understanding, see Figure 6.12 for a graphical verification of these wind vectors.

5.4. Population density geo-processing

Methods used in literature to estimate the presence of persons at a specific area, use population density data. Because population density data is often linked to residential addresses, which are never linked to office and industrial locations. Therefore, they assume industrial areas to be completely unpopulated, while especially during office hours, most of the population leave their homes and occupy offices, schools, and industrial areas. For this research, an assumption is made on the presence of people based on the presence of buildings.

Building area density Building density data can be obtained from difference data sources. Port of Rotterdam Authority geometry data does have building geometry data, but does not distinguish between industrial and residential buildings. The Netherlands' Cadastre has information available of different ground features in different resolutions, called 'TOPNL', with the lowest resolution data being named 'TOP1000NL', suited for creating maps with a scale of up to 1:1.5M, and 'TOP10NL', suited for scales upward from 1:5k. Although much lower resolution data than 'TOP10NL' is needed, as vector polygon accuracy is desired rather than pixel resolution, the lower resolution data does not contain a difference between industrial and residential building geometry. 'TOP100NL' contains features labeled as 'populated area', but these do not include housing outside of city limits, and they do not take into account building density. Higher resolution contains data of every building in and around the city area, therefore the entire set of data is has to be parsed. The 'TOP10NL' data has a GML extension which is written in XML. An XML parser is written to parse and extract the required features, which are labeled 'Gebouw', 'FunctioneelGebied > bedrijventerrein', 'Plaats > woonkern'. features labeled 'bedrijventerrein' are polygons drawn around buildings that have an industrial use. Features labeled 'woonkern' are polygons drawn around buildings that have a residential function. The 'Gebouw' feature contains geometry of all buildings.

The building geometry is converted to a density map, by estimating the density of building area for a specific ground type. For every building the polygon feature that defines the bounds of the geometry is determined, and converted to a point raster feature, with point spacing of 1 meter. By finding the intersection between the building polygon and the rectangular point grid a set of points is obtained. Combining the points for the entire set of industrial and residential buildings, a set of points is obtained representing a 1 m^2 presence of buildings.

The resulting building point distribution is used to generate a density map of building area density. For each grid cell j the number of points are counted, similar to the method of counting crashes.

Population density determination After a building area density map is generated, a factor is determined with the help of expert opinion of how much more persons will be present in residential areas, compared to industrial areas. When multiplying this factor with the building density, the total number of persons must be approximate the total number of inhabitants in the considered area, assuming that an equal number of people move out of residential areas located inside the considered area at the start of the day, as move into industrial areas and offices from outside the borders of the considered area.

Numbers of total number of inhabitants per area are registered by Statistics Netherlands (CBS). Every year a total number of inhabitants per square 500 meters and per square 100 meters is available for download. The total number of inhabitants $\sum_{j\,pop}\left[\rho(y_{i\,pop})\right]$ is estimated by summing the number of inhabitants of the j_{pop} grid cells within the bounding box that surrounds the industrial and residential building geometry.

An estimate is made for each building type, on what the population density is for the geometry. First, total building areas A_I, A_R, and ,A_T for each building type 'residential', 'industrial' and 'terrain' are obtained respectively, summing over the grid cells G_j. Secondly, fractions f_I, f_R and f_T are determined on how much of the total population resides at the area type locations at the daytime that the operation takes place. ($f_I + f_R + f_T = 1$) Finally, the population densities per area of area type ρ_I, ρ_R, and ρ_T are obtained, using the following formula:

$$\rho_A = \frac{A_A}{f_A * \sum_{j_{pop}}\left[\rho(y_{i_{pop}})\right]} \tag{5.28}$$

By multiplying the determined density value with the building area of each grid cell G_j, an estimate of population density per grid cell $\hat{\rho}_j$ results.

6

Model Verification

Before being able to discuss the results from chapter 7, several aspects of the model are verified in this chapter. Model flight dynamics are verified first by producing graphs of the UA state vectors. Subsequently, the flight dynamics of the crash event are verified in a similar fashion. Finally, the generation of the Dryden model wind turbulence samples is checked by generating a time series, and showing the distribution of the samples in a histogram.

6.1. Position verification of nominal flight conditions

The position state vector of nominal flight can verified by plotting horizontal position data on a map, overlain with the planned trajectory flight legs, as shown in Figure 6.1a. Due to the large area encapsulated by the nominal flight trajectory, it is difficult to see the blue graph of the traveled path appear underneath the orange line of the planned flight trajectory. Close-ups of the navigation performance near the sharp angled flight path direction changes near Port of Rotterdam Authority headquarters, and near the obtuse angled ones near the coast are shown in Figure 6.1b and Figure 6.1c respectively.

Vertical position verification is achieved by plotting the vertical position data along the axis pointing towards the east, as can be seen in Figure 6.2 and Figure 6.3.

The dynamic and three dimensional performance is best confirmed with a three dimensional animation, which can be reproduced with the python code used for this thesis. A screenshot of this animation is shown in Figure 6.4. Traveled and planned flight paths are shown in the same colors as the two dimensional graphs displayed above, and an outline of the coastlines is plotted in gray as a base layer. Due to the flight altitude of 120m being quite low, it is hard to distinguish the flight path being elevated from the base layer. It is however best seen at the take-off area shown as a blue dot in the top of the figure.

6.2. Uncontrolled descent verification

The model is started and run with thrust and steering control forces zero, $S_{c,t} = 0$, $T_t = 0$. The nose of the aircraft drops due to not being able to maintain airspeed, and the gravitational acceleration overcoming the lift acceleration, which decreases

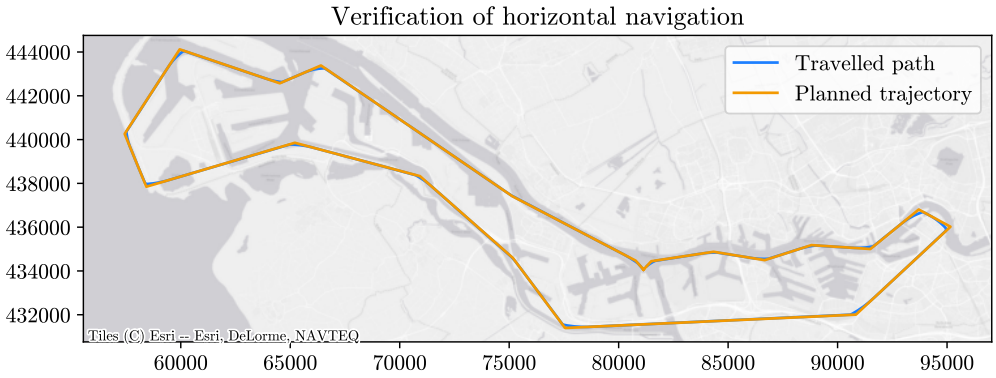

(a) Overview of the entire trajectory

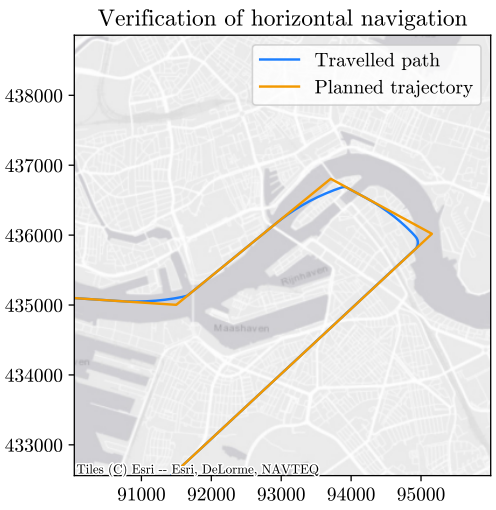

(b) Close-up area around World Port Center.

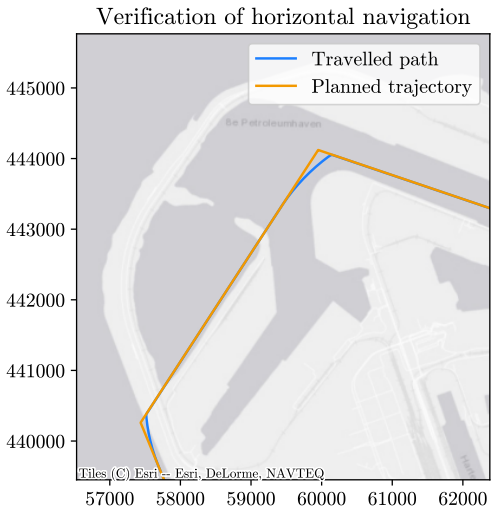

(c) Close-up Maasvlakte 2 area.

Figure 6.1: Flight path following and switch to next waypoint procedure performance of the flight model.

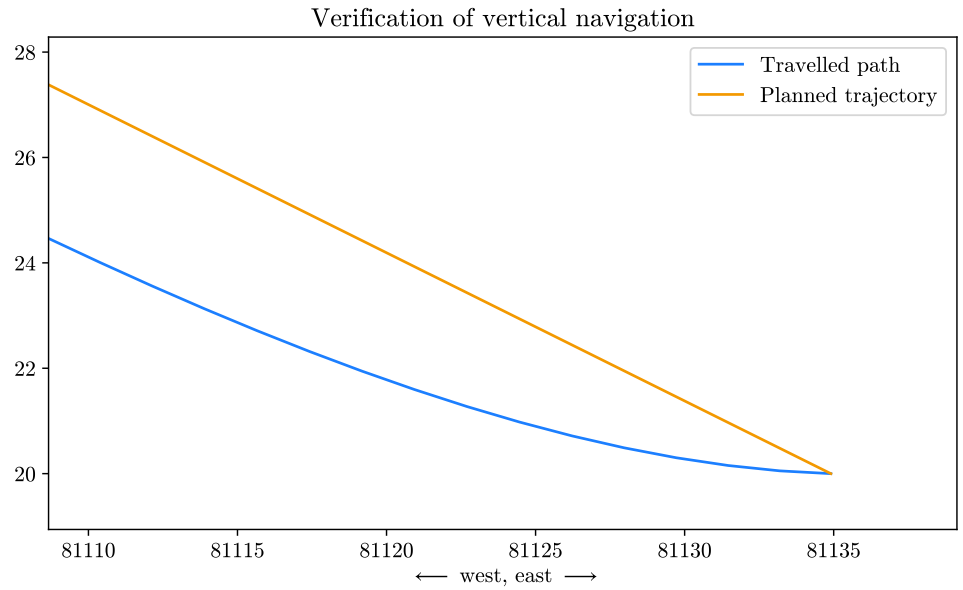

Figure 6.2: Verification of climb path navigation after take-off. Travel direction is to the left, as the x-axis displays the eastern coordinate.

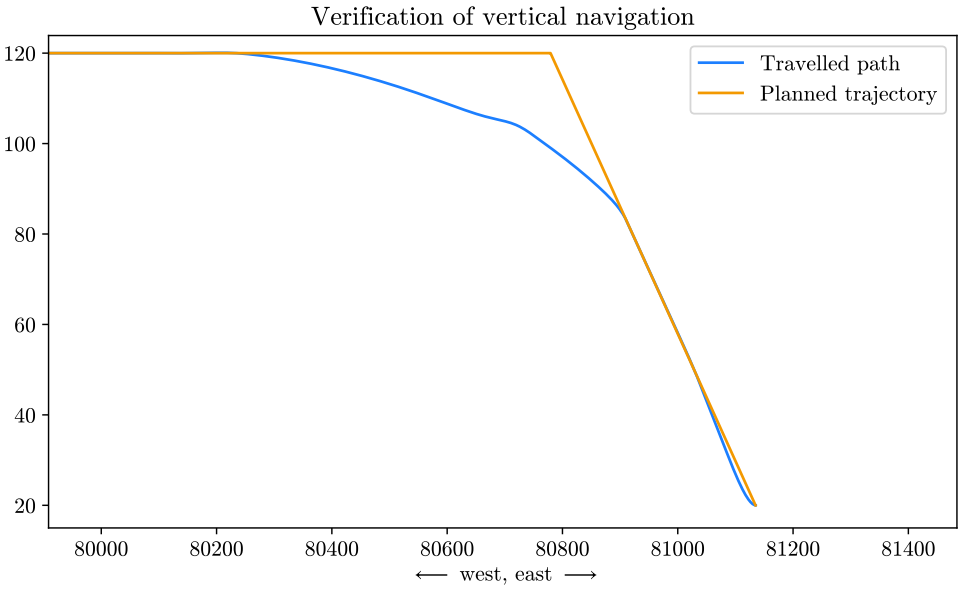

Figure 6.3: Verification of cruise path navigation while leveling off. Travel direction is to the left, as the x-axis displays the eastern coordinate.

as airspeed decreases. As a result, the airspeed vector gradually lines up with the gravitational acceleration vector that is pointed downwards. This results in the aircraft speeding up, increasing the lift acceleration, which in turn makes the nose of the aircraft point upwards again. This results in an ongoing oscillation called the 'phugoid', which normally occurs also in trimmed flight, when the aircraft is trimmed for a certain airspeed, usually triggered by a sudden elevator control input. The phugoid oscillation

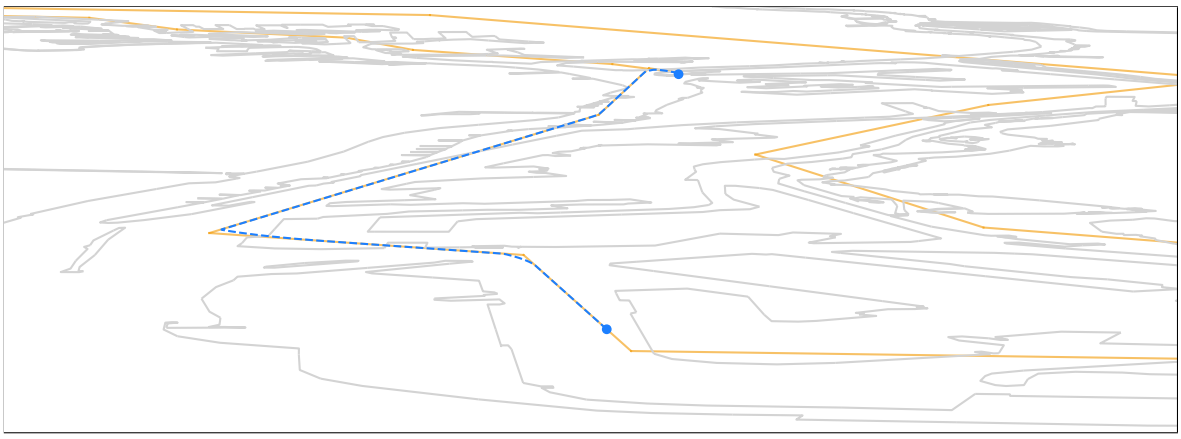

Figure 6.4: Screenshot of 3D simulation.

continues until the aircraft reaches the ground. For this research it is assumed that obstacles and ground elevation differences can be neglected due to the flat nature of the level surface around the seaport area. Crash locations are stored at the end of every failure simulation run. The crash locations are plotted in a map, as a first step in calculating the probability of a crash at a specific location.

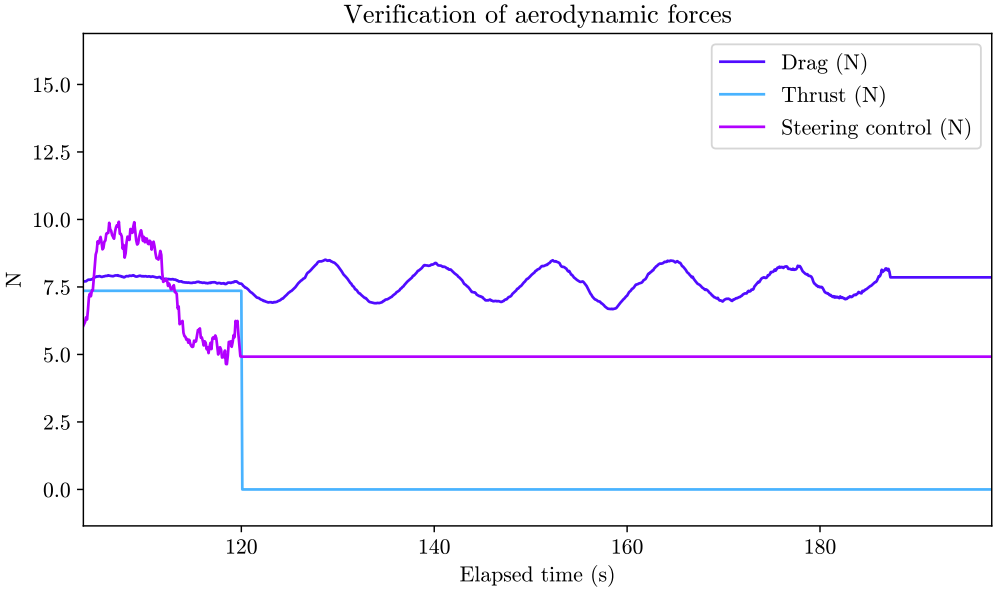

Figure 6.5: Verification of thrust and control vector failure.

Figure 6.5 shows thrust failure at a time t_f of 120 seconds into the flight. The constant thrust level for cruise is recorded to have value zero from t_{fail} onward. The continuously adjusting steering control vector is frozen after time t_{fail}. The magnitude of the drag force vector oscillates as a result of the airspeed fluctuating during the descent, which is further elaborated on below.

The data from Figure 6.5 is shown together with altitude data in Figure 6.6. This shows the altitude loss of the aircraft, that is a direct result from the loss of thrust.

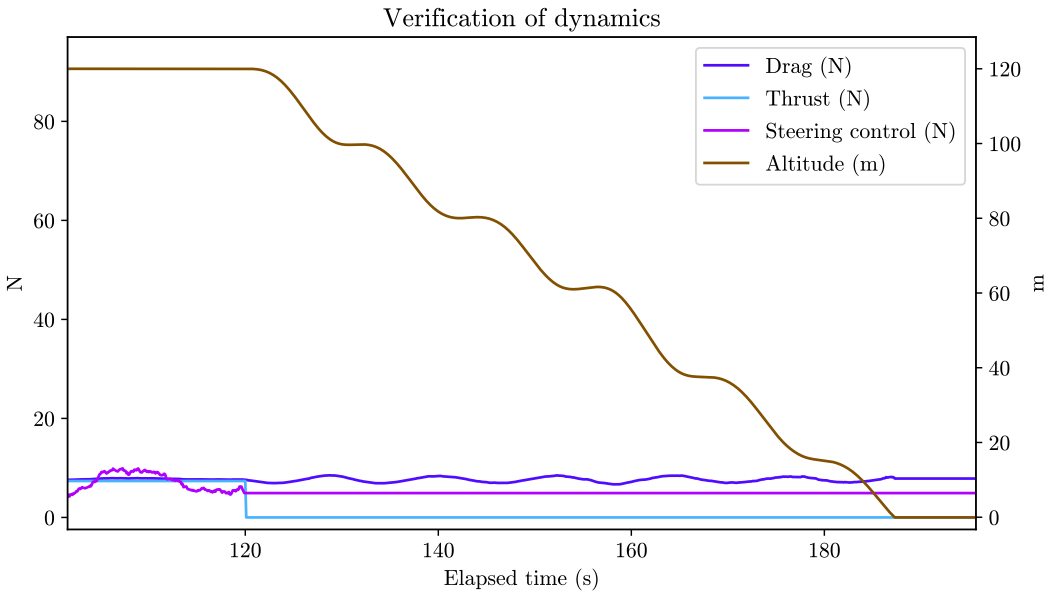

Figure 6.6: Altitude loss as a result of lost thrust.

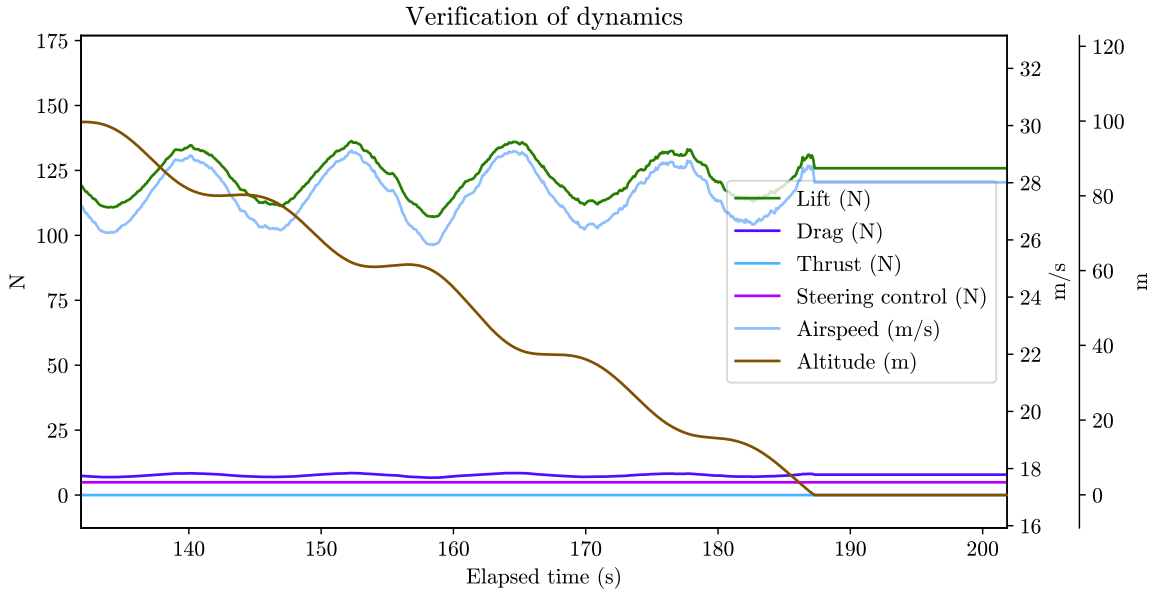

Figure 6.7: Relationship of altitude, airspeed, and lift oscillation.

It can be seen that the oscillations of the drag and lift force are synchronous with airspeed magnitude. This is expected as these forces are dependent on airspeed.

6.3. Wind turbulence generation verification

Working of the wind gust simulation model must be verified. The process implementation of the Dryden filter is checked first, after which the wind at ground estimation based on changing position and time is verified.

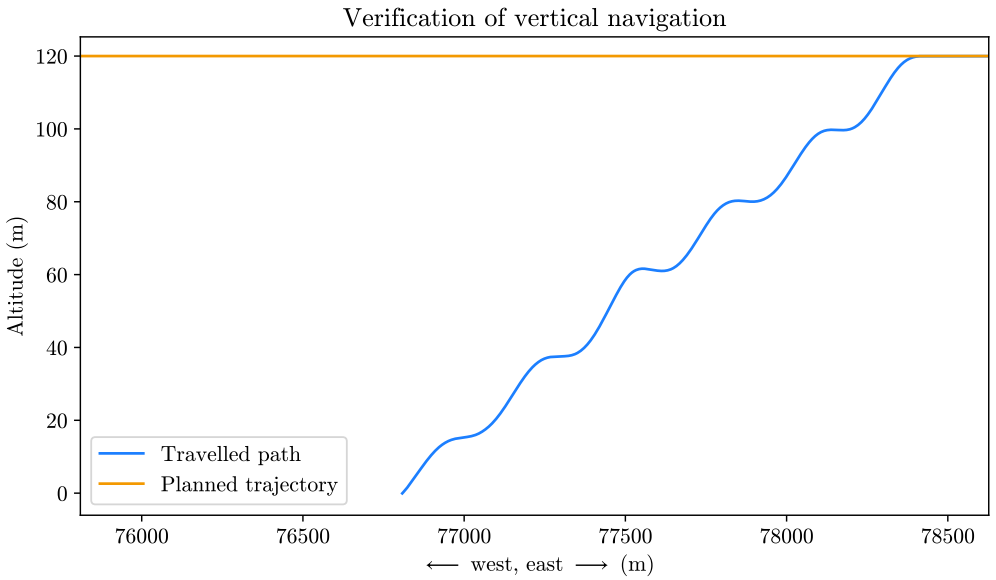

Figure 6.8: Glide trajectory displaying a phugoid oscillation. Travel direction is to the left, as the x-axis displays the eastern coordinate.

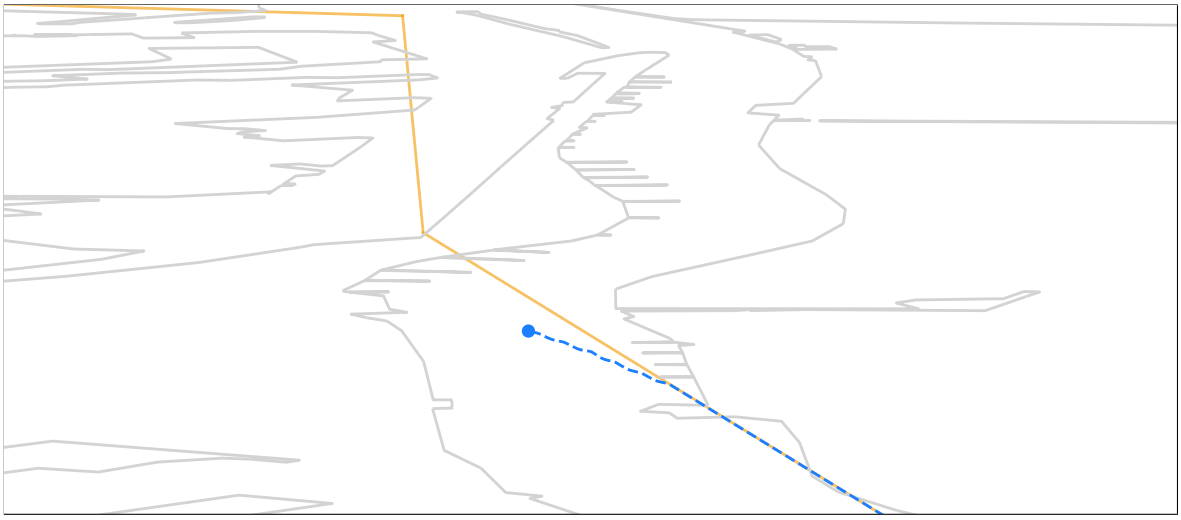

Figure 6.9: Three dimensional display of failure mode glide.

Filtering noise samples Figure 6.10 shows the generated discrete random white noise signal plotted together with the same sample used into Equation 5.23, at the same time point. This figure shows gradual movement around the mean gust magnitude, and also varying gust duration length. Gradual fluctuation of the gust signal ensures the aircraft not having to handle sudden wind velocity changes that would be unrealistic.

Representing the time series of the noise samples and the filtered signal by a histogram gives the graph displayed in Figure 6.11. It can be confirmed that the mean of the gray curve lies near zero, and the variance indeed being one. The resulting filtered signal looks similar to the Rayleigh distribution used by [Grimme, 2019].

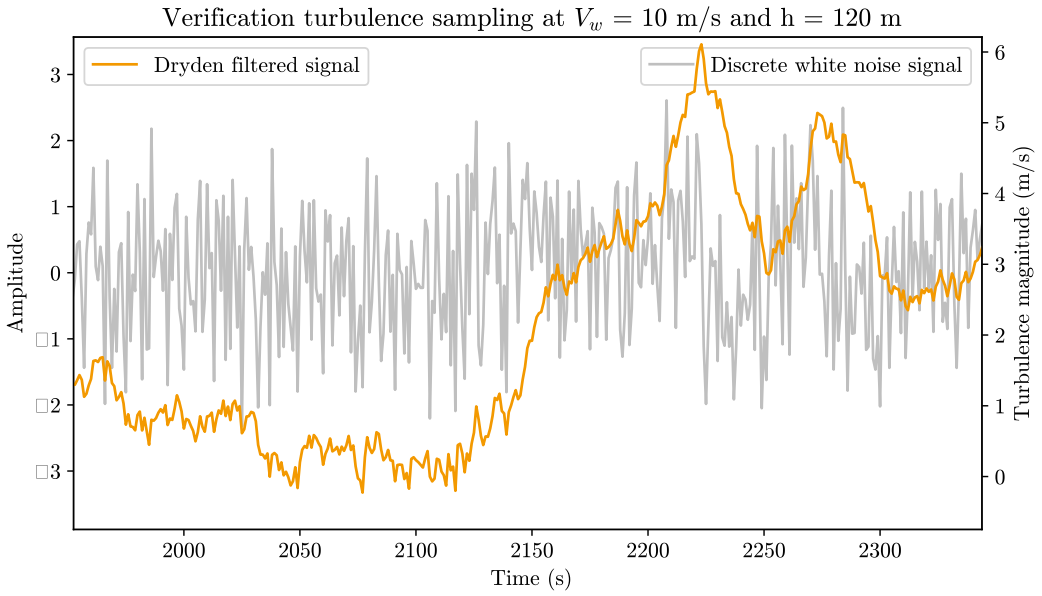

Figure 6.10: Verification of Dryden filter.

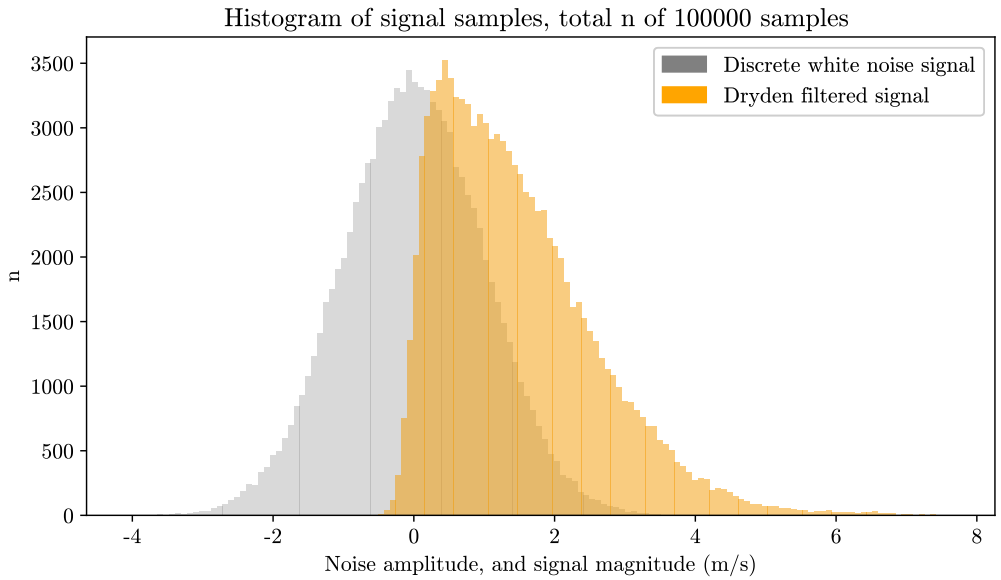

Figure 6.11: Histogram of discrete white noise and the filtered resulting signal from total number of draws n= 100000.

Wind estimation based on position The performance of the Equation 5.15 is displayed in Figure 6.12, where the magnitudes of the measurements of the ground stations are displayed. It can be clearly seen that the coastal wind measurements, indicated by a dark blue line, are higher in magnitude than the measurements of the station that is located more inland, indicated by a light blue line. The horizontal range of elapsed time that is displayed includes a range where the aircraft is on the returning leg, traveling from the coast inland. The red line indicates the estimated wind velocity at ground level, estimated from the projected coastal distance formula according to Equation 5.15.

This line clearly shows a decreasing wind magnitude as the aircraft travels towards the inland ground station.

In this graph, together with the ground wind vectors, the Dryden model simulated wind turbulence of the air surrounding the aircraft is displayed. The average magnitude of this simulated turbulence is a bit higher than the estimated ground wind vector, as the Dryden model corrects for height, which increases with altitude, as is implemented by [Grimme, 2019] with the help of the wind profile power law in the form of:

$$V_w(h) = V_{w_6}\left(\frac{h}{6}\right)^{\alpha}$$

which shows an increasing relation of wind magnitude as a function of height $V_w(h)$. V_{w_6} is the wind measured at 6 meters, h represents the altitude, α stands for the Hellman exponent which is a number between zero and one, based on the roughness of the terrain, and the stability of the air.

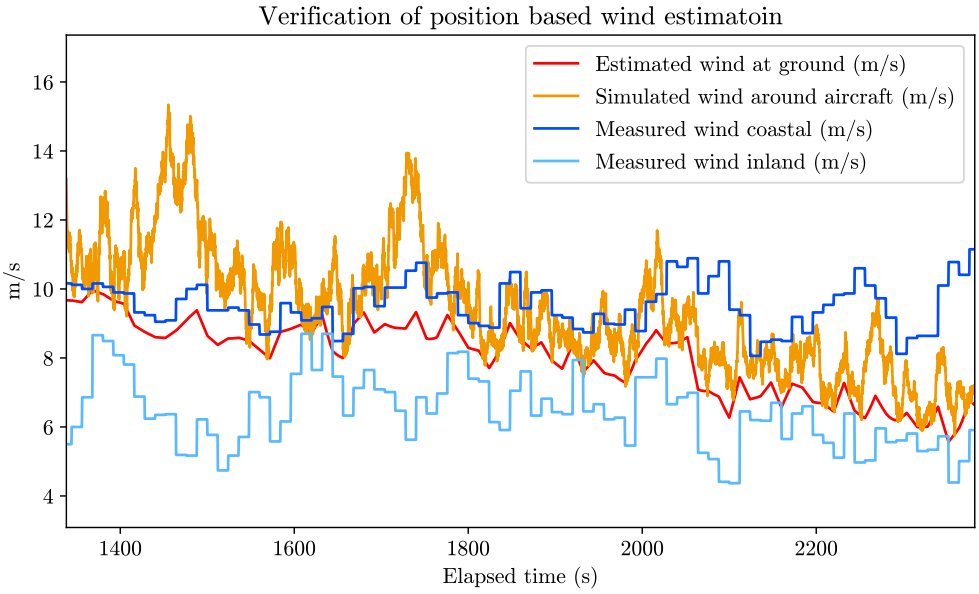

Figure 6.12: Verification of function that estimates wind based on position relative to wind measurement stations.

7

TPR Model Simulation

The simulation of the collective ground risk model that is described in chapter 5 is performed in this section. Pre-processing wind data and area specific Geographic Information Systems (GIS)-data, programming and running the model simulation, and visualizing results is done using the open source Python programming language (Python Software Foundation, https://www.python.org/).

The step wise approach from section 5.1 is used. As this description is applicable to a wide set of model characteristics, the subset used for this is first described. In this thesis the event of an uncontrolled glide is considered, $e = f$, rather than the entire set E of possible events. The assessment of the surveillance operation is aimed at the UA traveling a single nominal flight path. The set of i flights is therefore defined by $N = 1$. Only one d_i type is generated, because a single type of UA is used. Model input parameters are listed in Table 7.1.

7.1. Simulating crash probability density **Step 1 - 4**

For step 1, the four-dimensional nominal flight path is generated using the listed UA characteristics, the waypoints as listed in Table 7.2, and the nominal wind velocity vector $w_{t_{nom}}$, determined using the method of [Grange, 2014]. Measurements from KNMI are taken using the daily averages for the year 2019. The nominal wind velocity vector $w_{t_{nom}}$ for the inland station is calculated to be 2.68 m/s in eastern direction, and 2.57 m/s in northern direction, having a magnitude of 5.88 m/s. For the coastal station, $w_{t_{nom}}$ is determined to be 4.71 m/s in eastern direction, and 3.52 m/s in northern direction, having a magnitude of 5.88 m/s. Both of these calculated averages are measured at 6m of altitude, and corrected for coastal distance and altitude using the methods described in section 5.2. Nominal flight duration T_i^{nom} is generated as 3201.5 seconds.

Calculating the probability of a crash - Step 2 The failure rate $\lambda_{i,e}$ used for evaluating the probability of a crash for step 2 is obtained by using the advised failure rate for a small UA over a suburban area by [Melnyk et al., 2014], $\lambda_{i,e}$ = 9.14 * 10^{-5} failures per flight hour. Ideally, a measured failure rate would have been used for the risk assessment, but due to the novelty of unmanned aircraft systems this information is not

Parameters	Description	Value
General simulation parameters		
dt	Simulation time step	0.1 s
Fixed drone parameters		
m	Mass	12 kg
$T_{\max}$	Maximum thrust	25 N
T_{cruise}	Cruise thrust	7.36 N
$S_{\text{c, max}}$	Maximum steer force	100 N
C_{L}	Lift coefficient	0.32
C_{D}	Drag coefficient	0.016
S_S	Wing area	0.78 m^2
A_S	Frontal area	0.97 m^2
L_{UA}	Length	1.3 m
Nominal flight path generation		
$w_{t,inland}$	Inland station	[2.68, 2.57] m/s, Rotterdam Centrum (KNMI)
$w_{t,coastal}$	Coastal station	[4.71, 3.52] m/s, Hoek van Holland (KNMI)
Δt_w	Temporal resolution	None
trajectory	List of waypoints	See Table 7.2
Deviation simulation parameters		
$w_{t,inland}$	Inland station	Verkeerscentrale Lekhaven (Port of Rotterdam Authority)
$w_{t,coastal}$	Coastal station	Buitencontour Maasvlakte2 (Port of Rotterdam Authority)
Δt_w	Temporal resolution	12 s
trajectory	List of waypoints	See Table 7.2
s_0	Initial position	waypoint 1
v_0	Initial velocity	20(waypoint 2 - waypoint 1) / |(waypoint 2 - waypoint 1)|
θ_0	Initial heading	$\hat{v}_0$
Uncontrolled glide event simulation parameters		
$s_{0,e}^{i,k}$	Initial position	Sampled from empirical density function $s_t^{i,nom}$
$v_{0,e}^{i,k}$	Initial velocity	Sampled from empirical density function $v_t^{i,nom}$
$\theta_{0,e}^{i,k}$	Initial heading	$\hat{v}_{0,e}^{i,k}$
$w_{0,e}^{i,k}$	Initial wind vector	Sampled from empirical density function $w_t^{i,nom}$
λ	Failure rate	9.14 * 10^{-5} [Melnyk et al., 2014]
K	Number of simulations	K = 500000
Population density estimation parameters		
$\rho(y_{pop})$	Population census data	Statistics Netherlands (CBS)
A_I, A_R, A_T	Building area data	The Netherlands' Cadastre TOP10NL
f_I, f_R, f_T	Population fractions	0.19, 0.71, 0.1
bbox	Bounding box [xmin, xmax][ymin, ymax]	[55000, 99000], [425000, 440000]
Risk calculation parameters		
G_j	Grid cell dimensions	10m x 10m
DG	Average glide distance	24.7 m (1.8 m altitude)
DS	Stopping distance	1 m
S_I, S_R, S_T	Shelter factor	0.5, 0.5, 0

Table 7.1: Simulation parameters

Waypoints	East (m)	North (m)	Altitude (m)	Waypoints	East (m)	North (m)	Altitude (m)
waypoint 1	81135	434063	20	waypoint 12	77553	431396	120
waypoint 2	80779	434469	120	waypoint 13	90838	432006	120
waypoint 3	75140	437416	120	waypoint 14	95156	436019	120
waypoint 4	66403	443385	120	waypoint 15	93708	436806	120
waypoint 5	64523	442572	120	waypoint 16	91498	435003	120
waypoint 6	59951	444121	120	waypoint 17	88806	435181	120
waypoint 7	57437	440261	120	waypoint 18	86672	434495	120
waypoint 8	58427	437848	120	waypoint 19	84335	434876	120
waypoint 9	65209	439854	120	waypoint 20	81491	434444	120
waypoint 10	70924	438330	120	waypoint 21	81135	434063	20
waypoint 11	75166	434596	120				

Table 7.2: Trajectory containing three-dimensional waypoints

yet available. Using the $\lambda_{i,e}$, and the calculated T_i^{nom} of 3201.5 seconds, $P(e \mid i)$ from Equation (5.4) equals 8.13 * 10^{-5} crashes per flight.

Simulation of UA crashes - Step 3.1 A grid cell size of 100 m^2 is used to count the number of crash locations per grid cell. Every crash simulation starts with generating a random moment of event time t^k from a uniform distribution that is spanned from t_0 to T_i^{nom}, according to step 3.1. From each random event time a sample is drawn from the empirical densities for $s_{0,e}^{i,k}$, $v_{0,e}^{i,k}$, $\theta_{0,e}^{i,k}$ and $w_{0,e}^{i,k}$, which are acquired as described in the following paragraph. K = 500000 start times are generated.

Simulating deviation from nominal flight path - Step 3.2-3.3 Different simulations are performed to obtain the empirical density functions of the positional deviation ε_{te}^{S} to be used for the initial position $s_{t_e}^{i,k}$ in the uncontrolled flight event simulations in step 3.2. Deviation from the nominal flight path is determined by performing flight simulation under the influence of different wind magnitudes and stochastically generated wind turbulence. Subsequently the deviation is generated by simulating a GPS error, as performed by [Blom et al., 2020], to be able to compare the two methods. For the wind turbulence simulation, the widest time window of high temporal resolution wind measurement data that can be obtained from the Port of Rotterdam Authority database, has the length of a week. A week is chosen that measured wind conditions varying in wind magnitude and wind direction. Simulation of measurements during office hours is chosen so that the population estimation for industrial areas is consistent, instead of performing night time simulations resulting in collective ground risk estimates based on day time population of industrial areas, which has the potential to results in too conservative risk estimates. 500 flight simulations are performed with starting times generated from a uniform distribution across the wind velocity time series interval, resulting in 16 million state vector values. From the simulated nominal flight deviations, the empirical densities of $s_{t,e}^{i,k}$, $v_{t,e}^{i,k}$, $\theta_{t,e}^{i,k}$ and $w_{t,e}^{i,k}$ are obtained, as a function of the time t along the nominal flight path. K = 500000 start times are used to determine the initial states from these empirical densities, and are simulated to obtain an equal number of crash locations, by running the described flight model with $S_{c,t} = 0$, $T_t = 0$ according to step 3.3.

Estimating local crash density - Step 4 By dividing the number of crash locations per grid cell by the area of the grid cell according to Equation (5.9) from step 4, the probability density function of the crash location of the i^{th} UA flight $\hat{p}_s(y \mid i, e)$ is obtained. This probability density function is displayed in Figure 7.1. Close-ups of an industrial area and a residential area are shown in Figure 7.2a and Figure 7.2b respectively. A comparison against the probability density function of the crash location obtained from generating the deviation from the nominal flight path using the GPS error method is shown in Figure 7.3, and in the close-ups of Figure 7.4a and Figure 7.4b.

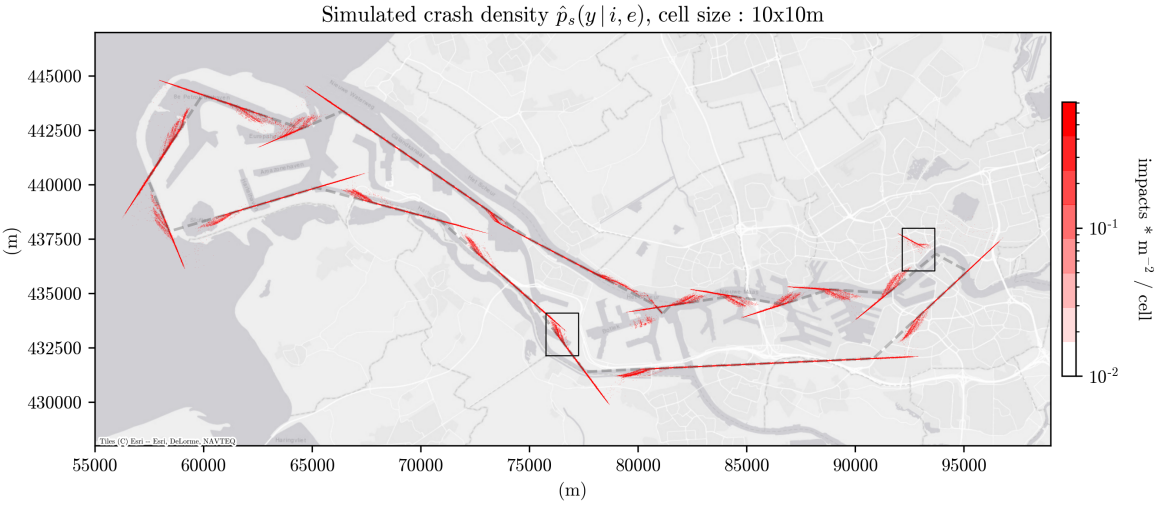

Figure 7.1: Map displaying wind turbulence model simulated local crash density $\hat{p}_s(y \mid i, e)$.

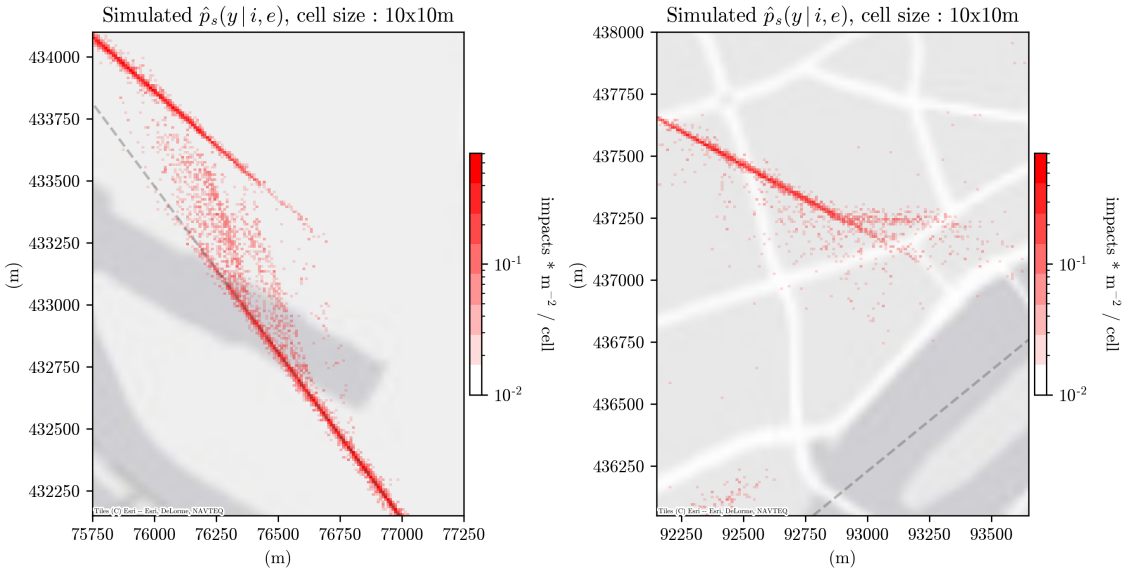

(a) $\hat{p}_s(y \mid i, e)$ Seinehaven close-up.

(b) $\hat{p}_s(y \mid i, e)$ city center close-up.

Figure 7.2: Close-ups of wind turbulence model simulated crash density $\hat{p}_s(y \mid i, e)$.

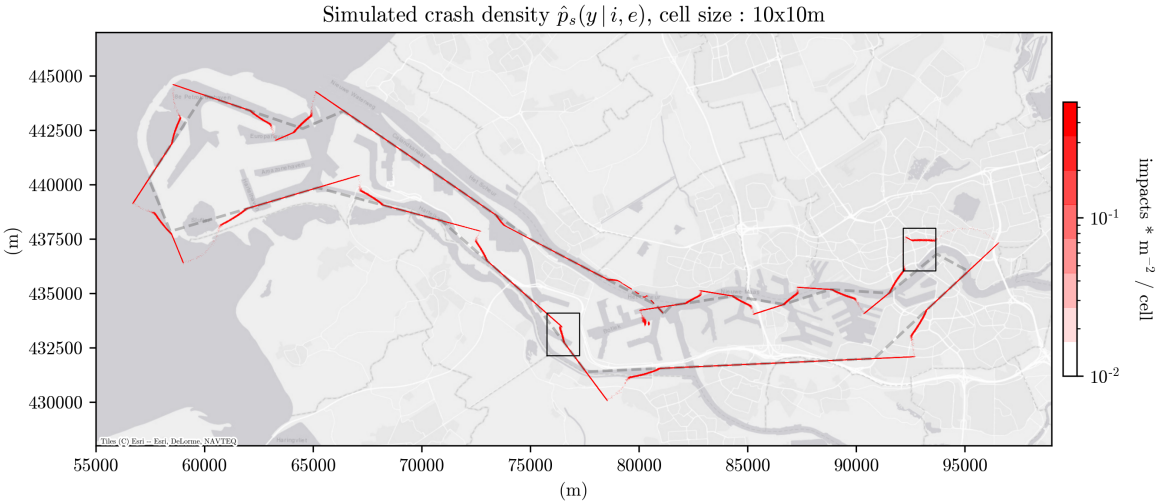

Figure 7.3: Map displaying GPS error model simulated local crash density $\hat{p}_s(y \mid i,e)$.

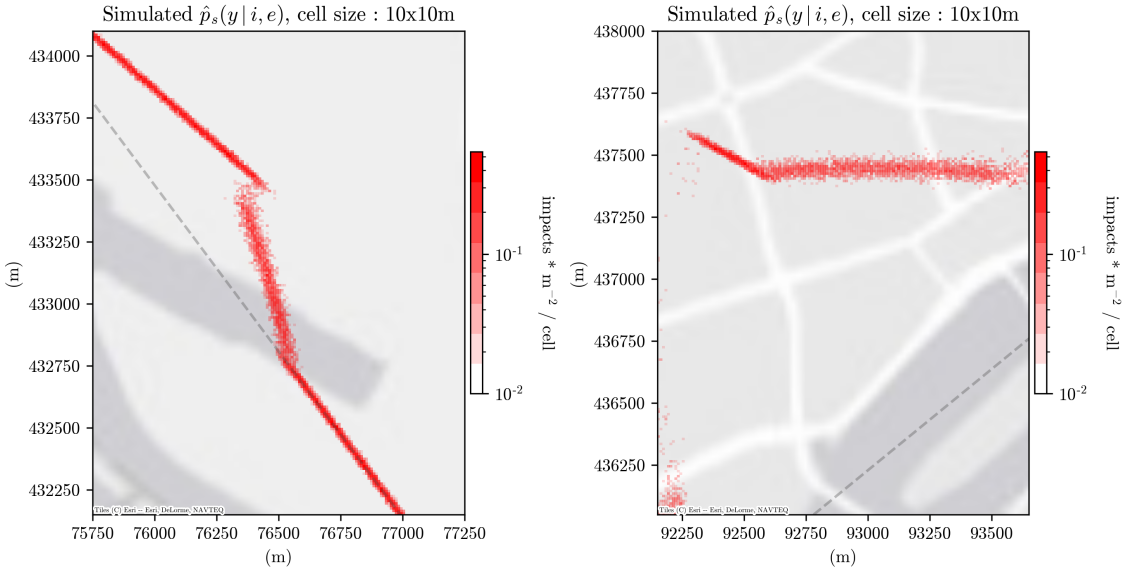

(a) $\hat{p}_s(y \mid i,e)$ Seinehaven close-up.

(b) $\hat{p}_s(y \mid i,e)$ city center close-up.

Figure 7.4: Close-ups of GPS error model simulated crash density $\hat{p}_s(y \mid i,e)$.

7.2. Estimating individual risk Step 5 - 6

Individual risk is estimated using Equation (5.12). Besides the calculated $\hat{p}_s(y \mid i,e)$ and $P(e \mid i)$ from the previous section, this equation also uses the impact area $|A(i,e)|$ and the probability of fatality $\hat{P}(F \mid j,i,e)$.

Probability of fatality - Step 5 The method for estimating the probability of fatality $\hat{P}(F \mid j,i,e)$ is taken from [Blom et al., 2020] using a probability of fatality model from [Range Commanders Council, 2001]. The probability of fatality method describes a relationship between kinetic energy and the probability of fatality. However, the high kinetic energy of the UA in this operation, in the considered horizontal flight mode,

results in a probability of fatality $\hat{P}(F \mid j,i,e)$ of 1, completing step 5.

Impact area - Step 6 Just like $\hat{P}(F \mid j,i,e)$, the method of [Blom et al., 2020] for the impact area $|A(i,e)|$ for step 6 is also used. $|A(i,e)|$ is described by [Range Commanders Council, 2001] as a 'lethal area L_A', and is determined based on the following equation:

$$L_A = (L_{UA}) + D_G + D_S + 2B) * (W_{UA} + 2B) \tag{7.1}$$

where L_{UA} is the length of the UA, W_{UA} the width of the UA, D_G the glide distance at 6 ft of altitude, D_S the stopping distance, and B represents one foot of buffer distance. Using a stopping distance of 1 meter, a glide distance of 24.7 meters (based on an average glide ratio of 13.5:1), and the vehicle parameters from Table 7.1, this results in an impact area $|A(i,e)|$ of 83.1 meters squared.

The results of steps 5 and 6 have the same value for every grid cell, and therefore the graphical representation of the relative values of each grid cell looks exactly the same. The color scale of Figure 7.1 can be multiplied with $P(e \mid i) * |A(i,e)| * \hat{P}(F \mid j,i,e) = 6.8 * 10^{-3}$ to obtain the result of $\hat{P}(F,j \mid i,e)$.

7.3. Obtaining population density Step 9

A plot of the building geometry data is displayed in Figure 7.5, showing where the industrial and residential areas are located in he seaport area. Using the method of estimating building density by converting these polygons to a grid consisting of points, the building density map is obtained, shown in Figure 7.6. Population census data is extracted from Statistics Netherlands (CBS) archives, of which the data is shown in Figure 7.7

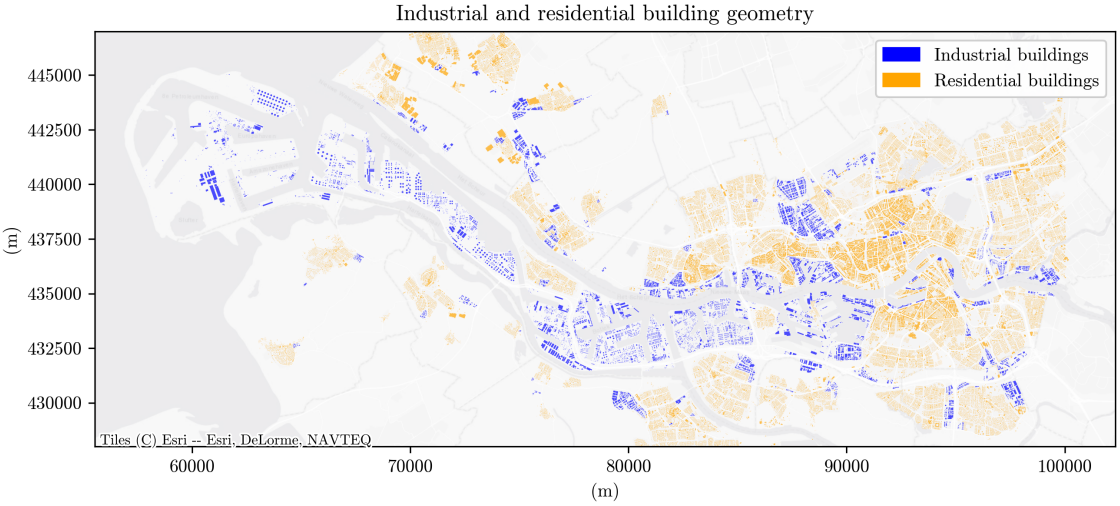

Figure 7.5: The Netherlands' Cadastre building geometry polygon data. Building geometry is separated into industrial and residential buildings.

The residential population distribution from the CBS, is used to estimate a population density based on the presence of all buildings, rather than just residential buildings. Population data is summed over the j_{pop} grid cells within the bounding box that surrounds the industrial and residential building geometry. Performing this summation

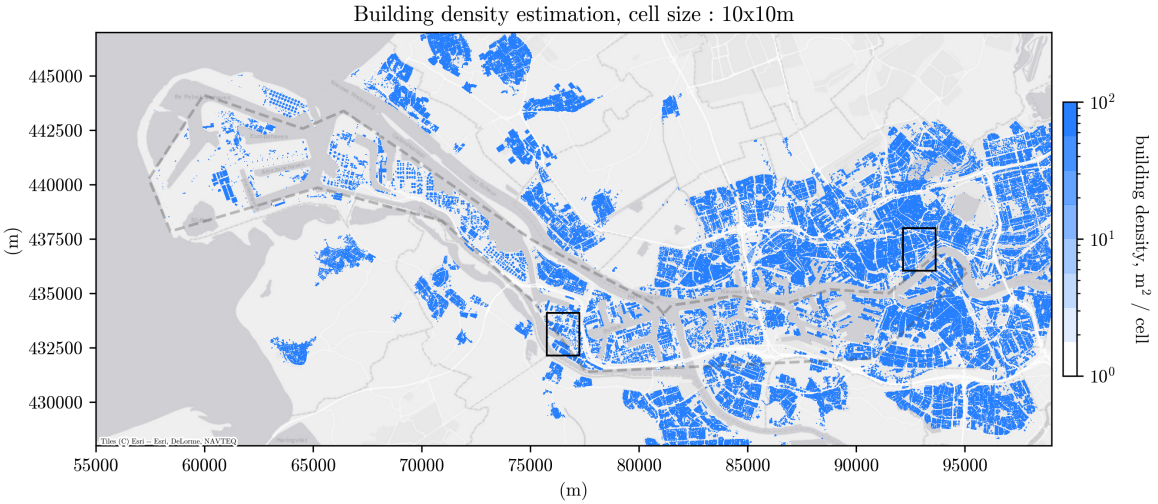

Figure 7.6: Approximation of building density.

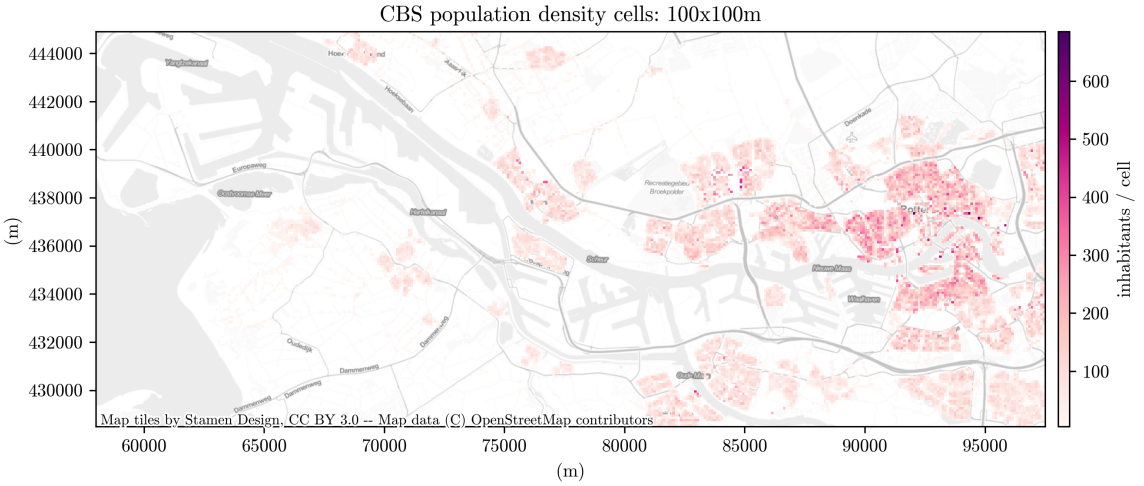

Figure 7.7: Statistics Netherlands data showing number of inhabitants per 100x100m grid cell.

for the grid squares within the bounds of the building geometry results in a total number of inhabitants of 916220. Building density comes down to 48.7 square kilometers of building summed over the 10 x 10 grid cells. Total residential building area equals 33.6 square kilometers. The total residential building area equals 15.1 square kilometers. Using Equation (5.28), a population density estimate is obtained for each ground area type. Table 7.3 shows the inputs used in the equation, and the resulting population density estimation. Figure 7.8 displays the estimated population density for each grid cell.

7.4. Estimation of collective ground risk **Step 10-13**

The collective ground risk is calculated by using Equation (5.13) in step 11. For this equation the probability of being sheltered needs to be taken into account.

Area type	Area (km^2)	Population	Fraction	Population density (km^{-2})	Shelter probability
Industrial area	$A_I = 15.1$	174082	$f_I = 0.19$	11528.6	$S_I = 0.5$
Residential area	$A_R = 33.6$	650516	$f_R = 0.71$	19360.6	$S_R = 0.5$
Terrain	$A_T = 975.8$	916220	$f_T = 0.1$	93.8	$S_T = 0$
Total	$A_{total} = 1025.2$	916220	$f_{total} = 1$	893.7	-

Table 7.3: Table displaying the population density and shelter probability per area type.

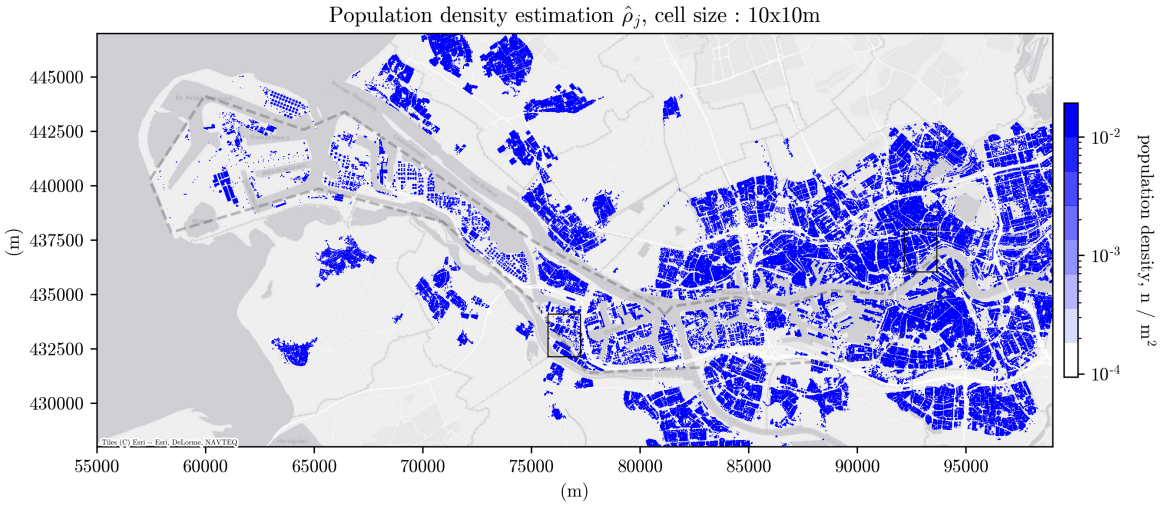

Figure 7.8: Approximation of population density $\hat{\rho}_j$.

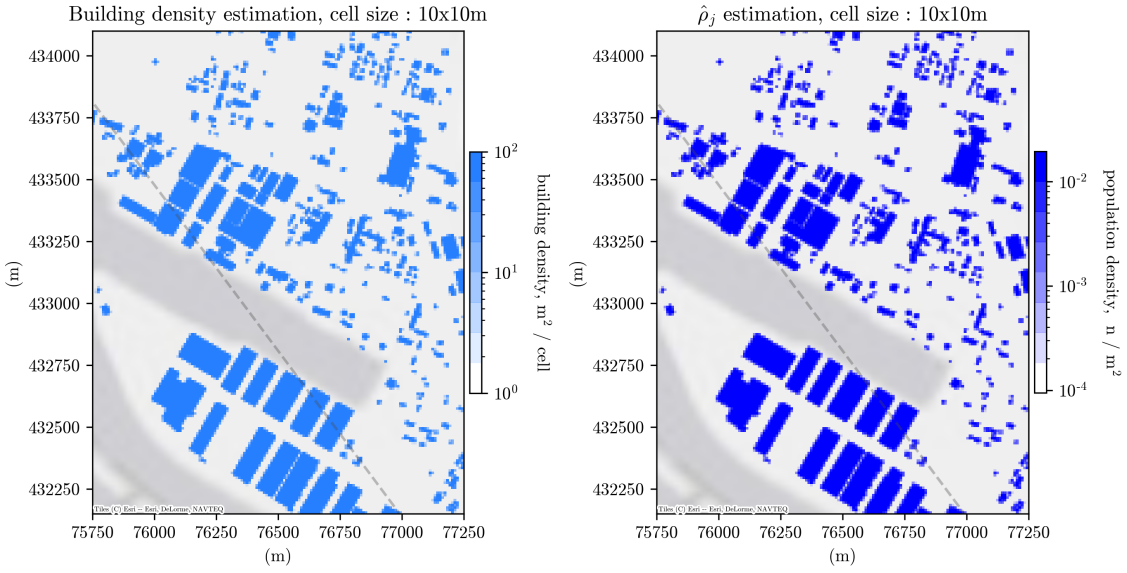

(a) Close-up of building density estimation. (b) Close-up of $\hat{\rho}_j$.

Figure 7.9: Population density estimation $\hat{\rho}_j$ close-ups of Seinehaven.

Shelter protection probability - Step 10 The shelter values that are used for step 10, are dependent of the building density in a grid cell, similar to how the population density is estimated based on building density. For both industrial buildings and residential buildings, the area of buildings inside a grid cell is related to a shelter factor

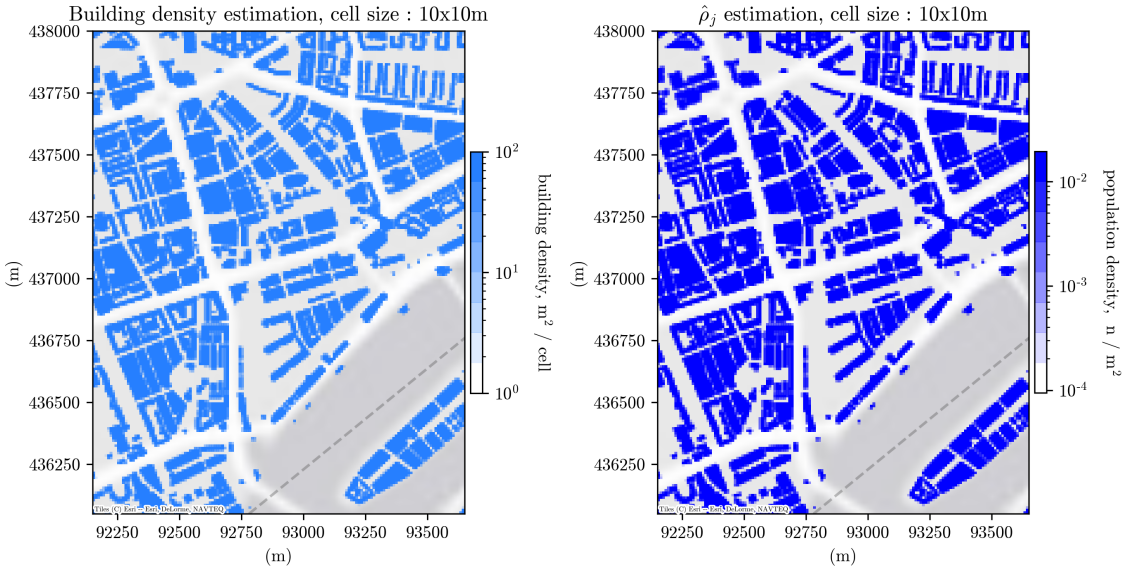

(a) Close-up of building density estimation.

(b) Close-up of $\hat{\rho}_j$.

Figure 7.10: Population density estimation $\hat{\rho}_j$ close-ups of the city center.

of 0.5, and for terrain, a shelter factor of 0 is used [Lum et al., 2011].

Estimated collective ground risk per flight hour - Step 11 - 13 Applying Equation (5.13) from step 11 for each grid cell, and dividing this value by the nominal flight duration T_i^{nom} according to step 12, the estimated collective ground risk $\hat{R}^i_{\text{Cground}}/T_i^{nom}$ per flight hour is obtained. The resulting collective ground risk per grid cell is shown in Figure 7.11. Summing the risk values over the grid cells results in a total $\hat{R}^i_{\text{Cground}}/T_i^{nom}$ of 3.84 * 10^{-6} casualties per flight hour based on a failure rate of 9.14 * 10^{-5} per flight hour. Comparing the simulated value of 3.84 * 10^{-6} casualties per flight hour for the considered event against the threshold level of the risk of the total operation, according to step 13, this results in a collective ground risk that exceeds the target of 1 * 10^{-6} by a factor of 3.8.

Figure 7.14 shows a histogram of the estimated collective ground risk grid cell values $\hat{R}^{i,j}_{\text{Cground}}$. The indicated threshold represents the value 1.75 * 10^{-11} that all grid cells that contain crash locations should average to meet the target level of safety of 1 * 10^{-6}.

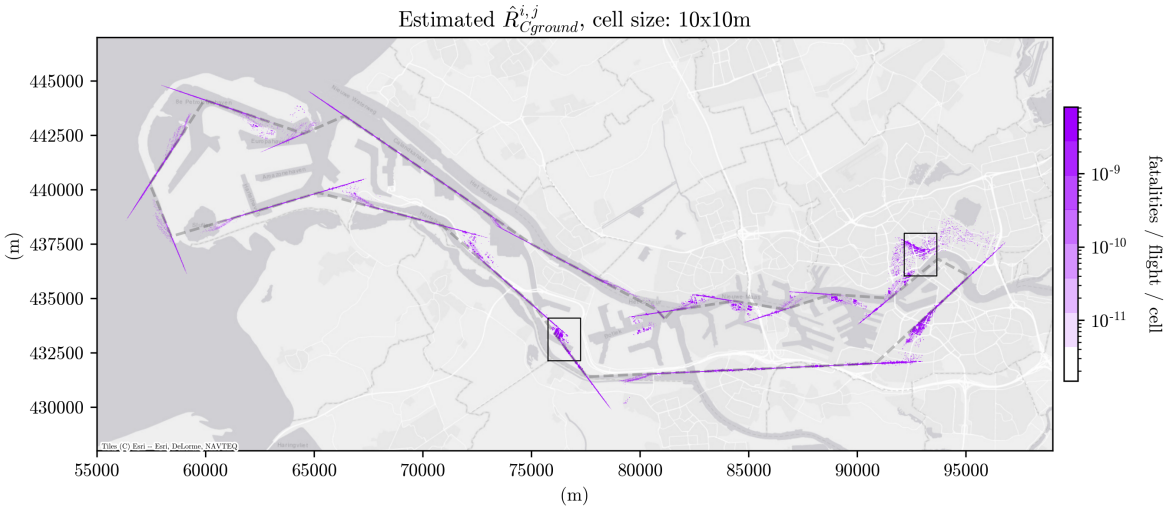

Figure 7.11: Estimated collective ground risk per grid cell $\hat{R}^{i,j}_{\text{Cground}}$

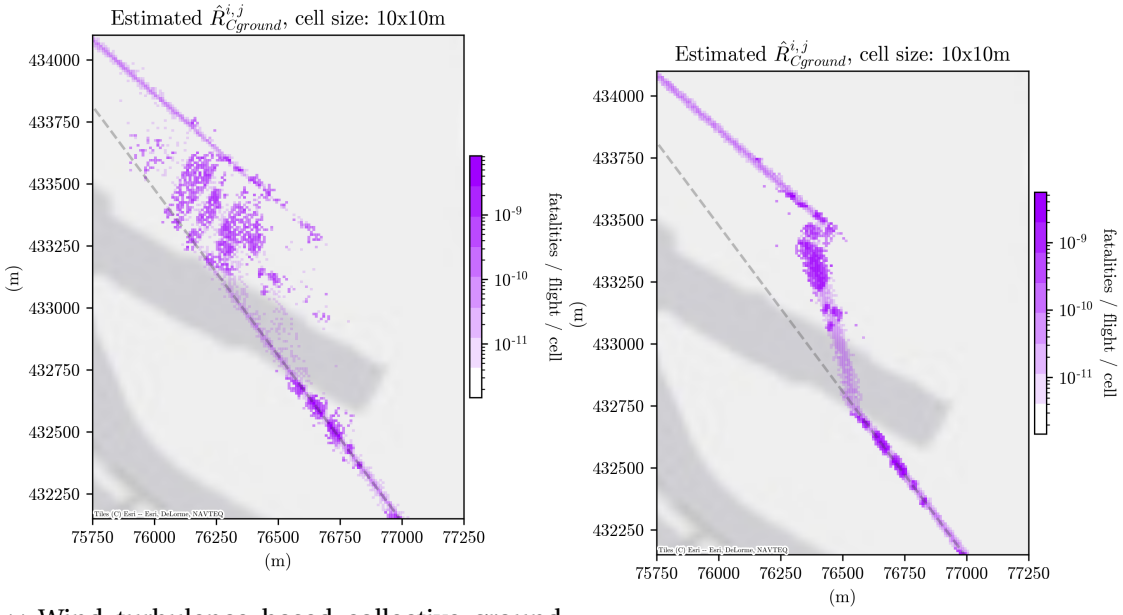

(a) Wind turbulence based collective ground risk.

(b) GPS error based collective ground risk.

Figure 7.12: Collective ground risk $\hat{R}^{i,j}_{\text{Cground}}$ close-ups of Seinehaven.

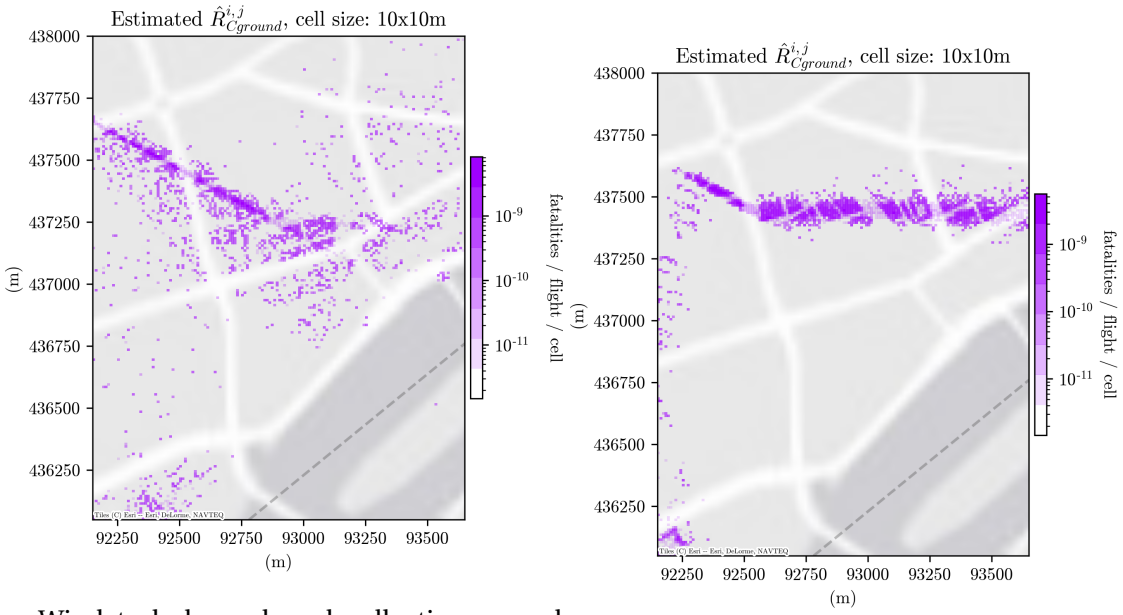

(a) Wind turbulence based collective ground risk.

(b) GPS error based collective ground risk.

Figure 7.13: Collective ground risk $\hat{R}^{i,j}_{\text{Cground}}$ close-ups of the city center.

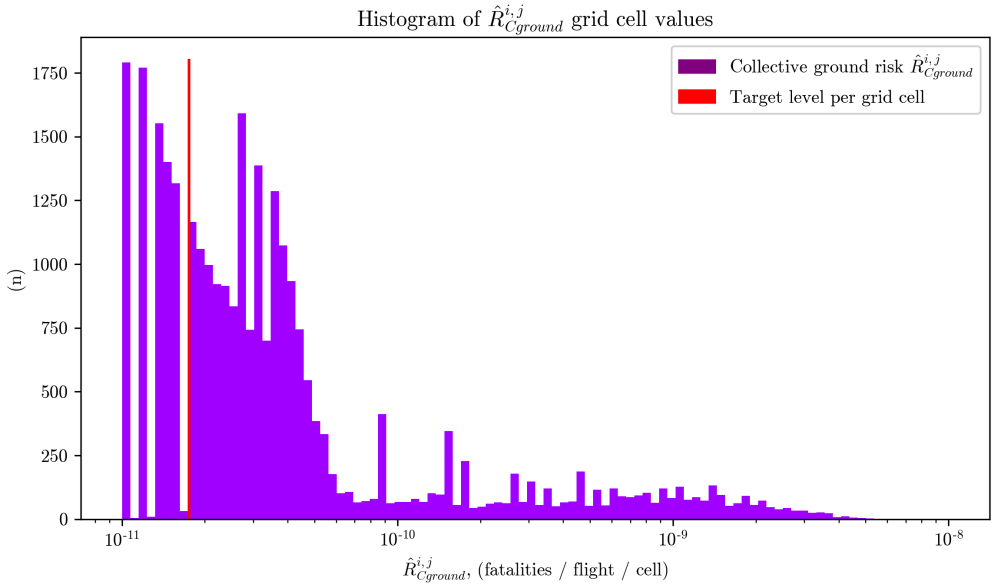

Figure 7.14: Histogram of estimated collective ground risk per grid cell $\hat{R}^{i,j}_{\text{Cground}}$

8

Discussion of Results

In this chapter the results of the quantification assessment are discussed. First, the results from the outcomes of several model steps from [Blom et al., 2020] are discussed. When doing a safety assessment of an operation, it is desired to be able to say something about the total level of safety. It must be noted that the assumptions from the scope of this research must be mentioned along with the calculated risk level. Although the simulated descent scenario is likely to be one of the bigger contributors to the collective ground risk per flight hour, the portion as a result from descent scenarios that are out of this thesis' scope add to the collective ground risk per flight hour. The calculated collective ground risk in this research should therefore not just meet the target level of safety, but should be well below this level.

8.1. Crash probability distribution

Several steps of the simulation results display some interesting aspects. The crash probability distribution consists of different recurring crash location distributions, consisting of lines, patches, and discontinuities.

Darker Patches The overall distribution of crash locations follows the nominal flight path trajectory, to a degree that the nominal flight path can roughly be distinguished. In the middle of the flight legs the crash distribution is a bit more confined within a region of a hundred meters. During the waypoint switch procedure, however, larger patches of crash distribution can be noticed in Figure 7.1, of which close-ups are shown in Figure 7.2. Although hard to show on a logarithmic color scale, these larger patches contain the same number of crash locations per forward traveled distance, and are just spread out in the direction perpendicular to the flight path that the UA is turning towards. These patches are highly influenced by the method of Equation (5.19), in terms of how aggressive the UA is programmed to pick up the nominal flight path, a procedure that is approximated in this thesis by Equation 5.19. The length of these patches are defined by the gradual turning to achieve a smooth pickup of the nominal flight path. The sooner the UA has picked up the nominal flight path, the sooner it is traveling in a straight line again, and the shorter the patch. The width of these patches is defined by the different wind velocities, a stronger head wind simulations result in a shorter glide distance, and stronger tailwinds result in a longer glide distance. As the UA

always glides roughly with the same glide ration relative to the airspeed, different wind velocities result in different glide path ground velocities, and thus different traveled ground distances.

Lighter patches The areas where the crash density seems to be 'discontinuous' in Figure 7.1 are the result from the first moment in the switch-to-next-waypoint procedure, where the UA has not picked up on its desired adjusted flight path vector $h_{AP,t}$ yet, and is steering with its maximum steering force into the direction of $h_{AP,t}$. Due to the quicker change in horizontal direction, compared to the situation described above, the crash locations are even more spread out, and therefore less visible. The reason that this lighter path seems to be absent in Figure 7.2a, is because the direction of the previous flight leg $h_{WP,t,previous}$ is not angled so much towards the direction of the new flight leg $h_{WP,t}$.

Denser lanes Regions where the nominal flight path is being followed, where the wider patches are absent and a thin lane seems to be shown, still have some spread of the crash locations. These can be attributed to the wind turbulence. Around the thinner lanes of the distribution of crash locations when flying the nominal straight line flight path, it can be observed that there is a maximum spread of about 50 meters. It can be assumed that this added spread of the crash locations due to wind turbulence is also likely to exist at the wider patch locations, although they cannot be distinguished here due to the more visible spread due to wind velocity. Note that the regions where the crash location distribution seems to overshoot the nominal flight path, are locations where the UA fails at the end of the nominal flight path, and therefore continues to glide in the trimmed direction, hitting the ground in a location under a virtual extended nominal flight path. The length of these overshoots appear to be longer than the regular glide distance, but what is seen mainly due to the logarithmic color scale in Figure 7.1 are the crash locations from the failure simulations with higher tailwind scenarios.

8.2. Risk estimation

The result of the final estimated collective ground risk density map displays some differences compared to the crash density map, due to the method of estimating population density, which are discussed below.

Building geometry It can be seen from Figure 7.11 that the darker patches near the coast are much lighter than the patches at the inland part of the trajectory near Rotterdam. This is because the ground ares of the darker patches near the city contain a lot of building geometry, whereas the coastal region still contains large areas of grassland. When looking at the close-ups of Figure 7.12a and Figure 7.13a, the geometry of the buildings can be distinguished amidst the data of the crash location distribution. It can be said that the population density estimation method has a too high resolution, as high risk values are shown inside a building geometry feature, while at this location the roof of the building is located, an area that is not likely to have persons present. When considering the collective ground risk over an area that encloses multiple buildings, these local inaccuracies are solved, and it can be assumed that these

have no effect on the summed level of collective ground risk over a the wider area.

Collective ground risk Summing up the values of each grid cell G_j results in a $\hat{R}^i_{\text{Cground}}/T_i^{nom}$ of 3.84 * 10^{-6} casualties per flight hour based on a failure rate of 9.14 * 10^{-5} per flight hour. Looking at the target level of safety per flight hour of 10^{-6}, this value is almost a factor 4 too high.

8.3. Comparison against GPS error model

Although the density map of the GPS error based nominal flight path deviation shows quite a different picture, having less wide patches, and more confined crash locations, the summation of the collective ground risk $\hat{R}^i_{\text{Cground}}/T_i^{nom}$ sums up to the same value of 3.84 * 10^{-6} fatalities per flight hour, having a deviation of only +0.09% compared to the wind turbulence based flight path deviation model.

9

Conclusions

This thesis has developed and applied a third party risk assessment to an unmanned aircraft systems-based surveillance operation in the port of Rotterdam.

9.1. Model extensions

During this thesis, the modeling and simulation approach has been extended in several ways:

- The details of an unmanned aircraft systems-based surveillance operation have been defined in collaboration with the Port of Rotterdam Authority.
- Fixed-wing UAS dynamics have been added to replace the existing quadcopter dynamic model.
- The influence of wind turbulence on the stochastic deviation of the drone flight has been modeled.
- A method has been developed for estimating local population densities, rather than using census-based data.

These models have been integrated in a Monte Carlo simulation of the operation subject to this thesis.

9.2. Simulation outcome

The total simulated level of collective ground risk of a failure resulting in an uncontrolled glide for the Port of Rotterdam Authority UAS surveillance operation is simulated to be $3.84 * 10^{-6}$ fatalities per flight hour, which answers the research question of this thesis. It exceeds the target level of safety of 10^{-6} fatalities per flight hour, based on the failure rate of $9.14 * 10^{-5}$ failures per flight hour, by a factor of 4.

When comparing this value to the multirotor TPR assessment due to a ballistic descent as a result from a failure, on which the applied TPR model is based, the factor that contributes the most to the assessed collective ground risk level is $|A(i,e)|$. The assessed crash impact area $|A(i,e)|$ is about eighty times higher due to the glide angle and the wing span of the fixed wing drone, compared to the multirotor. A comparison of the

wind turbulence based simulation of a deviation from the nominal flight path, to the GPS-based nominal flight path deviation simulation, shows that there is little effect of the deviation simulation method on the simulated collective ground risk value.

9.3. Follow up research

Two subjects are to be mainly addressed during future research, which are addressed below.

Based on the thesis simulation outcome, the concept surveillance operation can be subjected to a redesign iteration of the following aspects:

- The selected unmanned aircraft can be reconsidered, selecting one with more favorable characteristics such as a lighter maximum take-off weight, and shorter wing span.
- The trajectory can be adjusted to avoid areas that have been found to be highly populated.
- Mitigating measures can be designed to address the main contributors to the collective ground risk. (such as an emergency parachute)

Besides the design iteration, follow up research in the assessment of the surveillance operation is desired. To further answer the research question, several sub models can be improved:

- The estimation of the probability of failure of the system components of the selected unmanned aircraft must be improved.
- The failure simulation must be expanded to span the full set of failure events.
- The estimation of the probability of being sheltered must be improved for the various descent types.
- The population density estimation method must be tested, and be made dynamic based on daily commuting patterns of the population.

References

L. C. Barr, R. L. Newman, E. Ancel, C. M. Belcastro, J. V. Foster, J. K. Evans, and D. H. Klyde. Preliminary risk assessment for small unmanned aircraft systems. *17th AIAA Aviation Technology, Integration, and Operations Conference, 2017*, (July), 2017. doi: 10.2514/6.2017-3272.

S. Bertrand, N. Raballand, F. Viguier, and F. Muller. Ground risk assessment for long-range inspection missions of railways by UAVs. *2017 International Conference on Unmanned Aircraft Systems, ICUAS 2017*, pages 1343–1351, 2017. doi: 10.1109/ICUAS.2017.7991331.

H. A. P. Blom, C. Jiang, W. B. A. Grimme, M. Mitici, and Y. S. Cheung. Third party risk modelling of Unmanned Aircraft System operations , with application to parcel delivery service. 2020.

P. H. Bottelberghs. Risk analysis and safety policy developments in the Netherlands. *Journal of Hazardous Materials*, 71(1-3):59–84, 2000. ISSN 03043894. doi: 10.1016/S0304-3894(99)00072-2.

C. Brezoescu. Small lightweight aircraft navigation in the presence of To cite this version : HAL Id : tel-01060415 Thèse présentée pour l obtention du grade de Docteur de l UTC. 2014.

R. A. Clothier, B. P. Williams, and K. J. Hayhurst. Modelling the risks remotely piloted aircraft pose to people on the ground. *Safety Science*, 101(August 2017):33–47, 2018. ISSN 18791042. doi: 10.1016/j.ssci.2017.08.008. URL http://dx.doi.org/10.1016/j.ssci.2017.08.008.

A. L. Cour-Harbo. Ground impact probability distribution for small unmanned aircraft in ballistic descent. *2020 International Conference on Unmanned Aircraft Systems, ICUAS 2020*, (May):1442–1451, 2020. doi: 10.1109/ICUAS48674.2020.9213990.

K. Cunningham, D. E. Cox, J. V. Foster, S. E. Riddick, and S. A. Laughter. AirSTAR Beyond Visual Range System Description and Preliminary Test Results. *AIAA Guidance, Navigation, and Control Conference*, 2016. doi: 10.2514/6.2016-0882. URL https://arc.aiaa.org/doi/abs/10.2514/6.2016-0882.

Department Of Defense. Global Positioning System Standard Positioning Service. *Www.Gps.Gov*, (September):1 – 160, 2008. URL http://www.gps.gov/technical/ps/2008-SPS-performance-standard.pdf.

EUROCONTROL. Feasibility Study on the Integration of Third Party Risk near Airports into IMPACT. (June 2015), 2015. URL https://www.eurocontrol.int/sites/default/files/publication/files/d2-report-on-the-feasibillity-of-integrating-tpr-into-impact.pdf.

European Commission. Commission Delegated Regulation (EU) 2019/945 of 12 March 2019 on unmanned aircraft systems and on third-country operators of unmanned aircraft systems. (May 2019):C/2019/1821, 2019a. URL http://data.europa.eu/eli/reg_del/2019/945/oj.

European Commission. Commission Implementing Regulation (EU) 2019/947 of 24 May 2019 on the rules and procedures for the operation of unmanned aircraft. 2019: C/2019/3824, 2019b. URL http://data.europa.eu/eli/reg_impl/2019/947/oj.

S. K. Grange. Technical note : Averaging wind speeds and directions Technical note :. (October):12, 2014. doi: 10.13140/RG.2.1.3349.2006.

W. Grimme. *Modelling and Monte Carlo Simulation of the Third-Party Risk of Drones*. PhD thesis, 2019.

JARUS. SCOPING PAPER to AMC RPAS.1309. (2):1–38, 2015. URL http://jarus-rpas.org/sites/jarus-rpas.org/files/jar_04_doc_2_scoping_papers_to_amc_rpas_1309_issue_2_0.pdf.

JARUS. JARUS guidelines on Specific Operations Risk Assessment (SORA). page 48, 2017. URL http://jarus-rpas.org/sites/jarus-rpas.org/files/jar_doc_06_jarus_sora_v1.0.pdf.

C. Jiang, H. A. Blom, and A. Sharpanskykh. Third party risk indicators and their use in safety regulations for uas operations. *Aiaa Aviation 2020 Forum*, 1 PartF, 2020. doi: 10.2514/6.2020-2901.

J. M. Kai, T. Hamel, and C. Samson. A unified approach to fixed-wing aircraft path following guidance and control. *Automatica*, 108(October), 2019. ISSN 00051098. doi: 10.1016/j.automatica.2019.07.004.

KNMI. Daggegevens van het weer in Nederland, 2020. URL https://www.knmi.nl/nederland-nu/klimatologie/daggegevens.

A. La Cour-Harbo. Quantifying risk of ground impact fatalities of power line inspection BVLOS flight with small unmanned aircraft. *2017 International Conference on Unmanned Aircraft Systems, ICUAS 2017*, (October):1352–1360, 2017. doi: 10.1109/ICUAS.2017.7991323.

A. la Cour-Harbo. Quantifying Risk of Ground Impact Fatalities for Small Unmanned Aircraft. *Journal of Intelligent and Robotic Systems: Theory and Applications*, 93(1-2): 367–384, 2019. ISSN 15730409. doi: 10.1007/s10846-018-0853-1.

C. W. Lum, K. Gauksheim, T. Kosel, and T. McGeer. Assessing and estimating risk of operating unmanned aerial systems in populated areas. *11th AIAA Aviation Technology, Integration,and Operations (ATIO) Conference, including the AIAA Balloon Systems Conference and 19th AIAA Lighter-Than-Air Technology Conference*, (September), 2011. doi: 10.2514/6.2011-6918.

R. Melnyk, D. Schrage, V. Volovoi, and H. Jimenez. A third-party casualty risk model for unmanned aircraft system operations. *Reliability Engineering and System Safety*, 124:105–116, 2014. ISSN 09518320. doi: 10.1016/j.ress.2013.11.016. URL http://dx.doi.org/10.1016/j.ress.2013.11.016.

E. Petritoli, F. Leccese, and L. Ciani. Reliability and maintenance analysis of unmanned aerial vehicles. *Sensors (Switzerland)*, 18(9):1–16, 2018. ISSN 14248220. doi: 10.3390/s18093171.

Port of Rotterdam. Facts and figures of the port of rottrdam. 2019. URL https://www.portofrotterdam.com/sites/default/files/facts-and-figures-port-of-rotterdam.pdf.

S. Primatesta, A. Rizzo, and A. La Cour-Harbo. Ground Risk Map for Unmanned Aircraft in Urban Environments. pages 489–509, 2019.

Range Commanders Council. Range safety criteria for unmanned air vehicles - rationale and methodology supplement. *Range commanders council white sands missile range nm*, 2001.

E. A. Ranquist, M. Steiner, and B. Argrow. Exploring the Range of Weather Impacts on UAS Operations. *18th Conference on Aviation, Range and Aerospace Meteorology*, page 11, 2016.

Rijnmond. Kostbare drone van het leger crasht op Maasvlakte, 2020. URL https://www.rijnmond.nl/nieuws/197090/Kostbare-drone-van-het-leger-crasht-op-Maasvlakte.

SESAR JU. U-space blueprint - SESAR Joint Undertaking. 2017. doi: 10.2829/614891. URL https://www.sesarju.eu/u-space-blueprint.

H. Smets. Frequency distribution of the consequences of accidents involving hazardous substances in OECD countries. *Etudes et Dossiers*, 1996.

G. Stroe and I.-C. Andrei. Analysis Regarding the Effects of Atmospheric Turbulence on Aircraft Dynamics. *Incas Bulletin*, 8(2):123–132, 2016. ISSN 20668201. doi: 10.13111/2066-8201.2016.8.2.10.

United States Military. MIL-HDBK-1797B. *Change*, 2012.

A. Washington, R. A. Clothier, and J. Silva. A review of unmanned aircraft system ground risk models. *Progress in Aerospace Sciences*, 95(August):24–44, 2017. ISSN 03760421. doi: 10.1016/j.paerosci.2017.10.001. URL https://doi.org/10.1016/j.paerosci.2017.10.001.

A

Appendix A

	Hazard description	Likeliness
1	Power supply failure	2
2	Battery failure	3
3	GPS failure	2
4	Structural failure	2
5	Position communication failure	2
6	ATC system failure	1
7	Strong wind	5
8	Static obstacles programming failure	1
9	Dynamic obstacle communication failure	1
10	Visual object detection failure	3
11	Reduced visibility	4
12	Flight path programming failure	1
13	Control surface malfunction	2

	Scenario description	Likely root hazards / scenarios	Likeliness	Severity
1	Controlled glide	Scen: 6, 7	3	2
2	Emergency vertical landing	Scen: 7	4	1
3	Uncontrolled glide	Scen: 1, 15	2	4
4	Fly away	Scen: 15	2	4
5	Ballistic descent	Scen: 8	1	4
6	Vertical thrust failure	Scen: 9, 12	3	2
7	Horizontal thrust failure	Scen:10, 12	2	1
8	Airfoil damage	Scen: 14, 11	1	4
9	Vertical thrust rotor structural failure	Haz: 4	3	2
10	Horizontal thrust propeller structural failure	Haz: 4	2	1
11	Airfoil structural failure	Haz: 4	1	4
12	Engine power supply failure	Haz: 1 , 2, 7	4	2
13	Onboard electronics power supply failure	Haz: 1 , 2, 7	4	4
14	Mid-air collision	Scen 15, Haz: 5 ,6:	1	4
15	Unable to maneuver	Scen: 16, 17 Haz: 13	3	4
16	Automatic control failure	Scen:13, 18	4	2
17	Manual backup control compromised	Scen: 13, 19, 20	4	2
18	No position awareness of onboard system	Haz: 3, 8, 9, 12	2	4
19	No position awareness of supervisor	Haz: 3, 5, 8, 9, 11, 12	3	2
20	Control link failure	Haz: 5, 6	3	2

Table A.1: Tables of hazards and scenarios in the example event tree.

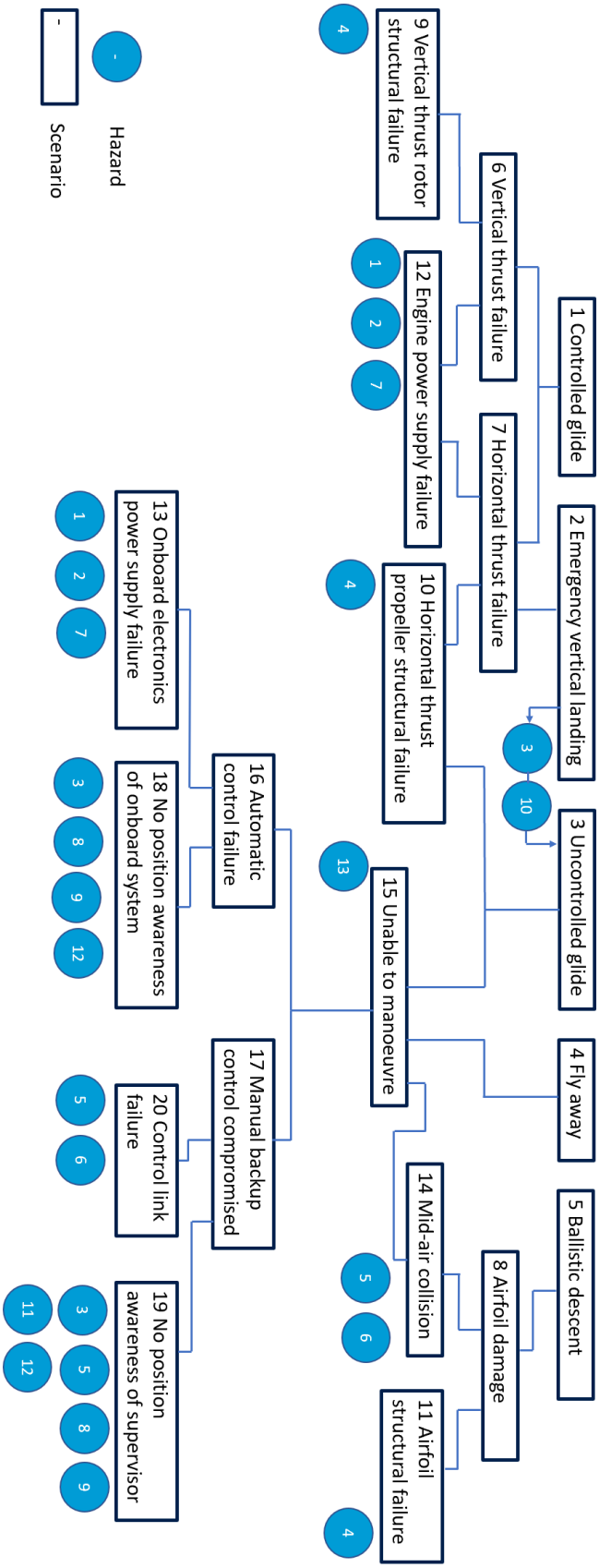

Figure A.1: Example of an event tree representation of the different hazards and scenarios.